Measurement Report: Distinct size dependence and diurnal variation of OA hygroscopicity, volatility, and CCN activity at a rural site in the Pearl River Delta (PRD) region, China

Mingfu Cai[1,2], Shan Huang[1*], Baoling Liang[3], Qibin Sun[3], Li Liu[4*], Bin Yuan[1], Min Shao[1], Weiwei Hu[5], Wei Chen[6], Qicong Song[1], Wei Li[1], Yuwen Peng[1], Zelong Wang[1], Duohong Chen[6], Haobo Tan[4], Hanbin Xu[3], Fei Li[4,7], Xuejiao Deng[4], Tao Deng[4], Jiaren Sun[2], and Jun Zhao[4,8,9]

[1] Institute for Environmental and Climate Research, Jinan University; Guangdong-Hongkong-Macau Joint Laboratory of Collaborative Innovation for Environmental Quality, Guangzhou, 511443, China

[2] Guangdong Province Engineering Laboratory for Air Pollution Control, Guangdong Provincial Key Laboratory of Water and Air Pollution Control, South China Institute of Environmental Sciences, MEE, Guangzhou 510655, China

[3] School of Atmospheric Sciences, Guangdong Province Key Laboratory for Climate Change and Natural Disaster Studies, and Institute of Earth Climate and Environment System, Sun Yat-sen University, Zhuhai, Guangdong 519082, China

[4] Institute of Tropical and Marine Meteorology of China Meteorological Administration, Guangzhou 510640, China

[5] State Key Laboratory of Organic Geochemistry and Guangdong Key Laboratory of Environmental Protection and Resources Utilization, Guangzhou Institute of Geochemistry, Chinese Academy of Sciences, Guangzhou 510640, China

[6] Guangdong Environmental Monitoring Center, Guangzhou 510308, China

[7] Xiamen Key Laboratory of Straits Meteorology, Xiamen Meteorological Bureau, Xiamen 361012, China

[8] Southern Marine Science and Engineering Guangdong Laboratory (Zhuhai), Zhuhai, Guangdong

27   519082, China

28   [9] Guangdong Provincial Observation and Research Station for Climate Environment and Air Quality

29   Change in the Pearl River Estuary, Guangzhou, Guangdong 510275, China

30   *Corresponding authors: Shan Huang (shanhuang_eci@jnu.edu.cn) and Li Liu (liul@gd121.cn)

31   Abstract.

32   Organic aerosol (OA) has a significant contribution to cloud formation and hence climate

33   change. However, high uncertainties still exist in its impact on global climate, owing to the varying

34   physical properties affected by the complex formation and aging processes. In this study, the

35   hygroscopicity, volatility, cloud condensation nuclei (CCN) activity, and chemical composition of

36   particles were measured using a series of online instruments at a rural site in the Pearl River Delta

37   (PRD) region of China in Fall 2019. During the campaign, the average hygroscopicity of OA (κ_{OA})

38   increased from 0.058 at 30 nm to 0.09 at 200 nm, suggesting a higher oxidation state of OA at larger

39   particle sizes, supported by a higher fraction of extremely low volatile OA (ELVOA) for larger size

40   particles. Significantly different diurnal patterns of κ_{OA} were observed between Aitken mode

41   particles and accumulation mode particles. For Aitken mode particles (30-100 nm), the κ_{OA} values

42   showed daily minima (0.02-0.07) during daytime, while the accumulation mode exhibited a daytime

43   peak (~0.09). Coincidently, a daytime peak was observed for both aged biomass burning organic

44   aerosol (aBBOA) and less oxygenated organic aerosol (LOOA) based on source apportionment,

45   which were attributed to the aging processes and gas-particle partitioning through photochemical

46   reactions. In addition, the fraction of semi-volatile OA (SVOA) was higher at all measured sizes

47   during daytime than during nighttime. These results indicate that the formation of secondary OA

48   (SOA) through gas-particle partitioning can generally occur at all diameters, while the aging

49   processes of pre-existing particles are more dominated in the accumulation mode. Furthermore, we

50   found that applying a fixed κ_{OA} value (0.1) could lead to an overestimation of the CCN number

51   concentration (N_{CCN}) up to 12%-19% at 0.1%-0.7% supersaturation (SS), which was more obvious

52   at higher SS during daytime. Better prediction of N_{CCN} could be achieved by using size-resolved

53 diurnal κ_{OA}, which indicates that the size-dependence and diurnal variations of κ_{OA} can strongly

54 affect the N_{CCN} at different SS. Our results highlight the need for accurately evaluating the

55 atmospheric evolution of OA at different size ranges, and their impact on the physicochemical

56 properties and hence climate effects.

1. Introduction

59   The impact of aerosol particles on global climate is widely known, including absorbing and

60 scattering solar radiation, and acting as cloud condensation nuclei (CCN). However, the extent of

61 their contribution on the climate forcing is still unclear. Organic aerosol (OA) as a dominant

62 component of fine particles (Jimenez et al., 2009), may contribute the uncertainties of climate effects

63 of particles, mainly owing to unknown sources, physical properties, formation, and aging

64 mechanisms (Volkamer et al., 2006; Kuang et al., 2020b; Rastak et al., 2017). Numerous studies

65 show that secondary organic aerosol (SOA) accounts for a large OA fraction in most atmospheric

66 environments (e.g., Huang et al., 2014; Shrivastava et al., 2017; Kanakidou et al., 2005; Hallquist

67 et al., 2009). Nevertheless, both primary OA (POA) and SOA in the ambient air remain poorly

68 characterized in terms of the formation mechanism and atmospheric evolution, and their particle

69 diameter can vary on a large scale. Their impact on the global climate and atmospheric chemistry is

70 still highly uncertain.

71   A combination of Aerodyne Aerosol Mass Spectrometer (AMS) or Aerosol Chemical Species

72 Monitor (ACSM) with positive matrix factorization (PMF) is widely used for investigating the OA

73 evolution in the atmosphere (Li et al., 2013; Huang et al., 2018; Huang et al., 2014; Chen et al.,

74 2015; Jimenez et al., 2009). For instance, Qin et al. (2017) found that hydrocarbon-like OA (HOA)

75 from traffic emission contributed up to 40% of OA during nighttime, owing to daytime traffic

76 restrictions on heavy vehicles in urban Guangzhou. Kuang et al. (2020a) reported a dominant

77 contribution to oxygenated OA (OOA) through aqueous-phase reaction in the North China Plain

78 (NCP). Guo et al. (2020) observed different SOA mechanisms between clean and pollution episodes

79 in the Pearl River Delta (PRD) region. Nevertheless, the investigation of bulk OA is still insufficient

80 in understanding the aerosol climate effects without the size-resolved characterization. The OA size

81 distribution is largely dependent on its composition, sources and aging level. Li et al. (2012)

82 observed various mass distribution patterns for different species in airborne particulate organics and

83 reported that dehydrated sugars, fossil fuel-derived n-alkanes, and PAHs showed a unimodal

84 distribution, while non-dehydrated sugars and plant wax was derived as n-alkanes which presented

85 a bimodal pattern. In the urban region, the Aitken mode was mainly dominated by HOA owing to

86 traffic emissions (Zhang et al., 2005b; Cai et al., 2020). In the marine atmosphere, the size

87 distribution of fine mode POA was found to be independent of sea salt, while coarse mode particles

88 tended to be internally mixed with sea salt (Gantt and Meskhidze, 2013). Similarly, the OA physical

89 properties were also found to be size-dependent. Deng et al. (2018) reported a higher OA

90 hygroscopicity ($\kappa_{OA} \approx 0.22$) at about 150 nm than that ($\kappa_{OA} \approx 0.19$) at sub-100 nm at a forest site. In

91 contrast, Zhao et al. (2015) measured size-dependent hygroscopicity and chemical composition for

92 SOA from various procedures and found that κ_{OA} of SOA from α-pinene photooxidation decreased

93 from 0.17 at 50 nm to 0.07 at 200 nm, which was attributed to the higher oxidation degree for

94 smaller particles.

95   The size dependence of OA properties in the aforementioned studies might exert impact on the

96   CCN prediction, which is mainly determined by their sources and formation processes. Cai et al.

97   (2018) found that N_{CCN} at 0.1% SS was underestimated by about 10% if a κ_{OA} value of 0.1 was used.

98   A model simulation from Liu and Wang (2010) showed that an increase of about 40-80% for the

99   CCN concentration was obtained by increasing the κ value of POA from 0 to 0.1. Wang et al. (2008)

100   reported that the uncertainties of the first indirect aerosol effect varied from -0.2 to 0.2 W m^{-2} for a

101   κ_{OA} value of 0 to 0.25. Rastak et al. (2017) showed that using a single-parameter framework of κ_{OA}

102   in evaluating the climate effects of aerosol could lead to significant errors (about -1.02 W m^{-2}),

103   which is the same order as the climate forcing of anthropogenic aerosol during the industrial period.

104   These results further highlight a need for the understanding of the relationship between the OA

105   evolution processes and its impact on the CCN activity at different particle sizes.

106   The OA hygroscopicity and volatility can provide information about the evolution of OA, given

107   that they are often related to the chemical composition of the particles. A positive correlation

108   between the hygroscopicity values and the oxidation degree of OA, including the ratio of atomic

109   oxygen to atomic carbon (O:C), the oxidation state ($\overline{OS_C}$), or the mass fraction of m/z 44 (for CO_2^+)

110   ion fragments in the organic spectra (f_{44}) from chemical composition, were widely reported in the

111   literature (Wu et al., 2013; Pajunoja et al., 2015; Chang et al., 2010). Kim et al. (2020) found that

112   the κ_{OA} was positively and negatively correlated with OOA and HOA at different size ranges,

113   respectively. Deng et al. (2019) reported a decreasing trend of κ_{OA} at a size range of 100-360 nm

114   during daytime in a forest environment, suggesting the formation of biogenic SOA (BSOA) through

115   photochemical oxidation of biogenic volatile organic compounds (BVOCs). The OA volatility,

116   specifically saturation vapor concentration (C^*), is linked to the gas-particle partitioning and aging

117   processes. In general, the C* value decreases with an increase of the oxidation degree and the

118   number of atomic carbon (Donahue et al., 2011). May et al. (2013) found that most of the biomass-

119   burning POA were semi-volatile. Saha et al. (2017) showed a lower volatility of OA in the afternoon

120   hours using a dual-thermodenuder (TD) system, probably owing to photochemical oxidation of OA.

121   Hong et al. (2017) derived the OA volatility distribution by a combination of the VTMDA

122   measurement and a multi-component evaporation dynamics model, and found a moderate (R≈0.4)

123   correlation between the OA groups obtained by the VTDMA data and the PMF results, respectively.

124   In this study, we investigate physical properties of OA at different size ranges, and evaluate

125   their influence on the atmospheric CCN concentration. A rural field measurement was conducted at

126   the Heshan site in the Pearl River Delta (PRD) region, China, during Fall 2019 (October and

127   November). The hygroscopicity, volatility, size-resolved CCN activity, and chemical composition

128   were measured by a series of online instruments. The size-resolved hygroscopicity and volatility

129   distribution of organics was investigated. PMF was employed to analyze the sources and processes

130   of OA. The impact of diurnal variation and size dependence of κ_{OA} on the N_{CCN} prediction at

131   different supersaturation (SS) was assessed.

132   **2.   Measurement and methodology**

133   **2.1 Measurement site**

134   The field measurements were conducted at the Heshan supersite in the Guangdong province,

135   China during autumntime 2019 (27th September to 17th November 2019). This supersite (22°42′39.

136   1″N, 112°55′35.9″E) is located at the southwest of the PRD region and surrounded by farms and

137   villages, with an altitude of about 40 m. All sample particles first passed through a Nafion dryer

138   (Model MD-700, Perma Pure Inc., USA) to maintain a relative humidity (RH) lower than 30%. The

139   schematic diagram of the experimental setup can be found in Fig. S1. Detailed descriptions of the

140   measurement site and some instruments can be found in Cai et al. (2021a).

2.2 Instrumentation

2.2.1   Aerosol hygroscopicity and volatility measurement

143   Size-resolved hygroscopicity and volatility of particles were measured by a H/V-TDMA

144   (model M3000, Bmet Inc., China). The instrument consists of two differential mobility analyzers

145   (DMA1 and DMA2, model 3081 L, TSI Inc., USA), a Nafion humidifier (Model MD-700, Perma

146   Pure Inc., USA), a heater tube, and a condensation particle counter (CPC, model 3788, TSI Inc.,

147   USA). The instrument was operated in H- and V- mode during the measurement with a cycle time

148   of about 3-4 h. The dried sample particles were firstly charged by an X-ray neutralizer and then

149   classified by DMA1 at six diameters (30, 50, 80, 100, 150, and 200 nm). In the H-mode, the chosen

150   particles with a specific dry diameter (D_0) were sequentially humidified by the Nafion humidifier

151   to achieve 90% of RH. A combination of DMA2 and CPC were employed to measure the size

152   distribution of humidified particles (Dp_{wet}). The hygroscopic growth factor (GF) at a certain dry

153   diameter can be defined as:

154    $$GF(D_0) = \frac{Dp_{wet}}{D_0} \qquad (1)$$

155   In the V-mode, the selected particles from DMA1 were heated in the heater tube at 100, 150,

156   200, and 250°C, respectively. Similar to the H mode, the size distribution of heated particles along

157   with particles at room temperature (25°C) was measured by the DMA2 and CPC. The volatility

158 shrink factor (VSF) at a certain diameter and temperature is then defined as:

159 $$VSF(T, D_0) = \frac{Dp(T)}{D_0} \tag{2}$$

160 Before the campaign, standard polystyrene latex spheres (PSLs; with a size of 20, 50, and 200

161 nm), ammonium sulfate, and sodium chloride were used to calibrate the diameter classification of

162 DMAs, hygroscopicity measurement, and the transport efficiency of particles in the heater tube,

163 respectively. For the H/V-TDMA data, the TDMAfit algorithm (Stolzenburg and McMurry, 2008)

164 was applied to fit the growth factor and volatility shrink factor probability density function (GF-

165 PDF and VSF-PDF) with various DMA transfer functions. The detailed data inversion processes

166 can be found in Tan et al. (2013a).

167 **2.2.2   The size-resolved CCN activity and particle number size distribution measurement**

168 A combination of a cloud condensation nuclei counter (CCNc, model 200, DMT Inc., USA)

169 and a scanning mobility particle sizer (SMPS, model 3938L75, TSI Inc., USA) was employed to

170 measure size resolved CCN activity. The supersaturation (SS) of each column (A and B) of CCNc

171 was set to be 0.1%, 0.2% and 0.4% (for column A), and 0.7%, 0.9% and 1.0% (for column B),

172 respectively. During the measurement, the SMPS was operated at a scanning mode. The sample

173 particles were firstly neutralized by an X-ray neutralizer (model 3088, TSI Inc., USA) and were

174 subsequently classified by a DMA. The classified particles were then split into three paths: one to a

175 CPC (model 3756, TSI Inc., USA) for measurement of particle number concentration (with a flow

176 rate of 0.6 LPM) and two to the CCNc for measurement of the CCN number concentration (N_{CCN})

177 at a specific SS (with a flow rate of 0.5 LPM).

178 The particle number size distribution (PNSD) in a size range of 1 nm-10 μm was measured by

179   a suite of instruments including a diethylene glycol scanning mobility particle sizer (DEG-SMPS,

180   model 3938E77, TSI Inc., USA), a SMPS (model 3938L75, TSI Inc., USA), and an aerodynamic

181   particle sizer (APS, model 3321, TSI Inc., USA). The detailed description of these instruments can

182   be found in Cai et al. (2021a). Before the measurement, the SMPSs were calibrated with PSLs (20,

183   50 and 200 nm) and the CCNc was calibrated with ammonium sulfate ($(NH_4)_2SO_4$) particles at

184   selected SSs (0.1%, 0.2%, 0.4%, 0.7%, 0.9%, and 1.0%, Sect. S1).

185   **2.2.3   Aerosol chemical composition measurement**

186   The size-resolved chemical composition of ambient aerosol particles was measured by a soot

187   particle aerosol mass spectrometer (SP-AMS, Aerodyne Research, Inc., USA). The principle and

188   operation of the instrument are generally the same as a high resolution time-of-flight aerosol mass

189   spectrometer (HR-ToF-AMS) (Canagaratna et al., 2007). In addition to an original tungsten

190   vaporizer (~600°C), a soot-particle module which mainly contains a Nd:YAG (1064 nm) laser was

191   integrated into HR-ToF-AMS for vaporizing refractory species (Onasch et al., 2012). As a result,

192   SP-AMS can provide chemical information for non-refractory species (nitrate, sulfate, ammonium,

193   chloride, and organics) as well as refractory species such as refractory black carbon (rBC) and

194   several metals. During the campaign, SP-AMS was run between V mode (only tungsten vaporizer)

195   and SP mode (tungsten and laser vaporizers) with a time resolution of 1 min. In order to minimize

196   disturbance caused by mode switch, 15 min averaged data are used in the present study. More details

197   on the quantification using ionization efficiency, composition dependent collection efficiency and

198   external instrument as well as software for SP-AMS data analysis could be found in Kuang et al.

199   (2021).

200   Facilitated by the time-of-flight chamber in SP-AMS, the particle mass size distribution can be

201   measured in submicrometer size range, specifically, 40 to 800 nm in vacuum aerodynamic diameter

202   (Dva). The mass size distribution for relevant AMS species was used in this study for investigating

203   the link between particle chemical composition and volatility/hygroscopicity. Since SP-AMS

204   provided the size distribution versus Dva, the equation below was used to convert Dva into mobility

205   diameter (Dp).

206    $$D_p = \frac{D_{va}}{S \times \frac{\rho_p}{\rho_0}}$$ (3)

207   where S is the shape factor, ρ_p is the particle density, and ρ_0 is the density for water (1 kg m^{-3}). In

208   this study, we estimate that the particles were close to sphere due to high RH in the PRD and thus a

209   shape factor of 0.8 was applied. An overall particle density of 1.6 kg m^{-3} is used.

210   Based on high resolution data from SP-AMS, source apportionment was performed for organic

211   aerosols (OA) in the bulk PM$_1$ with positive matrix factorization (PMF, Paatero, 1997; Paatero and

212   Tapper, 1994) following the instruction in Ulbrich et al. (2009). The input data, selection of solutions,

213   mass spectral profile, and time series of each factor can be found in Kuang et al. (2021). In brief,

214   OA measured at the Heshan site could be divided into six components with identified sources and

215   processes, including two from primary sources and four factors corresponding to secondary

216   formation: a hydrocarbon-like OA (HOA) contributed mainly by vehicle exhausts mixed with

217   cooking emissions, a biomass burning OA (BBOA) related to biomass burning combustion from the

218   surrounding villages, an aged BBOA (aBBOA), a more oxygenated OA (MOOA) from regional

219   transport, a less oxygenated OA (LOOA) provided by daytime photochemical formation, and a

220   nighttime-formed OA (Night-OA) related to secondary formation during nighttime.

2.3 Methodology

2.3.1   Estimates of hygroscopicity

The hygroscopicity parameter κ can be obtained under subsaturation condition by the H/V-TDMA measurement and supersaturation condition by the CCNc measurement. The κ value (κ_{HTDMA}) can be estimated from the growth factor measured by H/V-TDMA (Petters and Kreidenweis, 2007):

$$\kappa_{HTDMA} = (GF^3 - 1)\left[\frac{1}{RH}\exp\left(\frac{4\sigma_{s/a}M_w}{RT\rho_w D_p} - 1\right)\right] \tag{4}$$

where $\sigma_{s/a}$ is the surface tension of the solution/air interface and the solution is temporarily assumed to be pure water (0.0728 N m^{-1} at 298.15 K), M_w is the molecular weight of water (0.018 kg mol^{-1}), R is the universal gas constant (8.314 J mol^{-1} K^{-1}), T is the thermodynamic temperature in Kelvin (298.15 K), ρ_w is the density of water (about 997.04 kg m^{-3} at 298.15 K) and D_p is the particle diameter in meters.

For the CCNc measurement, the κ value (κ_{CCN}) is calculated from the critical supersaturation (Sc) and the critical diameter (D_{50}) by the following equation (Petters and Kreidenweis, 2007):

$$\kappa_{CCN} = \frac{4A^3}{27D_{50}^3(\ln Sc)^2}, A = \frac{4\sigma_{s/a}M_w}{RT\rho_w} \tag{5}$$

The critical diameter, D_{50}, is defined as the diameter at which 50% of the particles are activated at a specific SS, and can be obtained from the N_{CCN} and N_{CN} measured by the CCNc and SMPS system:

$$\frac{N_{CCN}}{N_{CN}} = \frac{B}{1 + \left(\frac{D_p}{D_{50}}\right)^c} \tag{6}$$

where the B and C are fitting coefficients.

241 **2.3.2   Derivation of the size-resolved hygroscopicity of organic matter**

242   The size-resolved chemical composition is adopted to derive the size-dependent hygroscopicity

243 of organic matter (κ_{OA}). However, the AMS cannot provide sufficient information of the size-

244 resolved species, especially for small size particles (< 100 nm) owing to the low mass concentration.

245 Thalman et al. (2017) proposed a method to reconstruct the size-resolved chemical composition,

246 which combines a time-resolved bulk mass concentration and an average mass distribution.

247 Nevertheless, the variation of mass distribution was not considered in this method. In this study, a

248 bimodal lognormal distribution function method was adopted, and the one-hour average mass

249 distribution was fitted to obtain the reconstructed size-resolved chemical composition. The average

250 mass distribution with bimodal lognormal fitted modes of each species was shown in Fig. S2.

251   According to the ZSR mixing rule (Zdanovskii, 1948; Stokes and Robinson, 1966), the

252 hygroscopicity of particles (κ_{AMS}) can be calculated based on the SP-AMS measurement, assuming

253 an internal mixing state for all particles:

254     $$\kappa_{AMS} = \sum_i \kappa_i \varepsilon_i \tag{7}$$

255 where κ_i is the κ value of each component and ε_i is the volume fraction of corresponding species in

256 particles. The mole concentrations of the inorganic species are estimated based on the NH_4^+, SO_4^{2-},

257 and NO_3^- measured by the AMS (Gysel et al., 2007):

258     $$n_{NH_4NO_3} = n_{NO_3^-}$$

259     $$n_{H_2SO_4} = max\ (0, N_{SO_4^{2-}} - n_{NH_4^+} + n_{NO_3^-})$$

260     $$n_{NH_4HSO_4} = min\left(2n_{SO_4^{2-}} - n_{NH_4^+} + n_{NO_3^-}, n_{NH_4^+} - n_{NO_3^-}\right)$$

261     $$n_{(NH_4)_2SO_4} = max\left(n_{NH_4^+} - n_{NO_3^-} - n_{SO_4^{2-}}, 0\right)$$

262      $n_{HNO_3} = 0$ (8)

263   where n denotes the number of moles of each component (NH_4^+, SO_4^{2-} and NO_3^-), ε_{org} and ε_{BC}

264   were obtained from mass concentration measured by the SP-AMS. The density and κ value of each

265   component were listed in Table 1.

266   The κ_{OA} can be calculated based on the size-resolved chemical composition and H/V-TMDA

267   measurement using following equation:

268      $\kappa_{OA} = \dfrac{\kappa_{HTDMA} - (\kappa_{inorgsalt}\varepsilon_{inorgsalt} + \kappa_{BC}\varepsilon_{BC})}{\varepsilon_{org}}$ (9)

269   **2.3.3**   **Volatility data**

270   During the heating process, some particles could be lost between DMA_1 and DMA_2 due to

271   complete evaporation (CV), thermophoresis, and Brownnian diffusion (Philippin et al., 2004).

272   Owing to these losses, the V-mode measurement does not represent the actual volatility distribution

273   of the monodisperse particles. The sodium chloride (NaCl) particles, which do not evaporate at the

274   set temperature in this measurement, were used to determine the particle losses owing to

275   thermophoretic forces and diffusion. The size- and temperature-dependent transmission efficiency

276   ($\eta(D_p, T)$) of NaCl in the heater was shown in Fig. S3. Thus, the number fraction of CV group

277   ($NF_{CV}(D_p, T)$) at a certain diameter and temperature can be calculated using the following equation

278   (Cheung et al., 2016):

279      $NF_{CV}(D_p, T) = 1 - \dfrac{N'(D_p, T)}{N(D_p)\eta(D_p, T)}$ (10)

280   where $N'(D_p, T)$ is the number concentration of particles at a specific diameter and temperature

281   after heating, which was measured by the CPC in the H/V-TDMA. The $N(D_p)$ is the number

282   concentration of particles with a diameter D_p before heating, which was provided by the SMPS

283   measurement. The volume fraction remaining (VFR) after heating for the measured particles can be

284   obtained according to the following equation:

285    $$VFR(D_p, T) = \sum_i VSF_i^3(D_p, T)\, NF_i(D_p, T)[1 - NF_{CV}(D_p, T)] \tag{11}$$

286   where i represents the ith VSF bin, and NF_i is the number fraction of particles with VSF_i, which is

287   calculated based on the VSF-PDF ($c(VSF, D_p, T)$):

288    $$NF_i = \int_{VSF_i}^{VSF_{i+1}} c(VSF, D_p, T)\, dVSF \tag{12}$$

289   The mass fraction remaining (MFR) was assumed to be proportional to VFR, assuming that

290   the density of particles was constant before and after heating.

291   **2.3.4   Multi-component evaporation dynamics model**

292   Based on the volatility basis set (VBS) framework (Donahue et al., 2011), the organic matter

293   was classified into three organic groups based on the saturation concentration (C*(T_{ref}),

294   T_{ref}=298.15 K): extremely low volatility organic aerosol (ELVOA, C^*=10^{-5} µg m^{-3}), low volatility

295   organic aerosol (LVOA, C^*=10^{-2} µg m^{-3}), and semi-volatility organic aerosol (SVOA, C^*=10 µg m^{-}

296   ^{3}).

297   A multi-component evaporation dynamics model described by Lee et al. (2011) was used to

298   simulate the evaporation of particles in the heated tube of the H/V-TDMA by solving the mass

299   transfer regime equation, in order to obtain the size-resolved distribution of the aforementioned

300   three OA groups. The MFR, residence time (about 4.11 s) in the heater tube, the temperature of the

301   heater tube, particle number concentration, particle sizes, chemical composition, and

302   thermophysical properties of each species (Table 2) were input into the model. The particles were

303   assumed to be internally mixed with organic and inorganic species, including three organic groups,

304   NH$_4$NO$_3$, (NH$_4$)$_2$SO$_4$, and black carbon (BC). The mass transfer of each component i between the

305   aerosol and gas phases in the transition regime was calculated from the following equation:

306    $\frac{dm_{p,i}}{dt} = 2\pi D_i D_p f(Kn, \alpha)(C_{i,g} - f_i C_i^*(T) exp(\frac{4\sigma_{s/a} M_i}{D_p \rho_i RT}))$

307    $\frac{dC_{i,g}}{dt} = -\frac{dm_{p,i}}{dt} N_p(D_p)$ (13)

308   where $m_{p,i}$ (μg) is the mass of species i in a single particle, $C_{i,g}$ (μg m^{-3}) is its gas-phase

309   concentration, D_i (m^2 s^{-1}) is the diffusion coefficient for species i in air, D_p (m) is the particle

310   diameter, $f(Kn, \alpha)$ is a correction term to account for non-continuum mass transfer depending on

311   Knudsen number (Kn) and mass accommodation coefficient (α), f_i is the mole fraction of species

312   i, $C_i^*(T)$ is the saturation concentration at temperature (T) of the heater tube, M_i (kg mol^{-1}) is the

313   molecular weight of species i, ρ_i (kg m^{-3}) is its density and $N_p(D_p)$ (cm^{-3}) is the number

314   concentration of particles with a diameter D_p.

315   The correction term $f(Kn, \alpha)$ is determined by the following equation (Seinfeld and Pandis,

316   2016):

317    $f(Kn, \alpha) = \frac{1+Kn}{1+2Kn(1+Kn)/\alpha}$

318    $Kn = \frac{2\lambda_i}{D_p}$ (14)

319   where λ_i is the mean free path of species i in the air, which is defined as $\lambda_i = \frac{2D_i}{c_i}$. The c_i is the mean

320   speed of species i and $c_i = \sqrt{\frac{8RT}{\pi M_i}}$.

321   The temperature-dependent $C_i^*(T)$ is estimated from the Clausius-Clapeyron equation:

322    $C_i^*(T) = C_i^*(T_{ref}) exp\left[\frac{\Delta H_{vap,i}}{R}\left(\frac{1}{T_{ref}} - \frac{1}{T}\right)\right]\frac{T_{ref}}{T}$ (15)

323   where $\Delta H_{vap,i}$ (kJ mol^{-1}) is the enthalpy of vaporization. The known mass fractions of NH$_4$NO$_3$,

324   (NH$_4$)$_2$SO$_4$, and BC were calculated respectively, based on the SP-AMS measurement. The time

325   step of the model was set to be 10^{-3} s. The characteristics of each species were listed in Table 2. The

326   mass fraction of each organic group in different particle sizes was derived by minimizing the squared

327   residuals (SSR) values, $SSR = \sum_{T_i=T_1}^{T_5}[MFR_{model}(T_i, Dp) - MFR_{measured}(T_i, Dp)]^2$. The non-

328   linear constrained optimization function "fmincon" in MATLAB (version 2016a, Mathworks Inc.)

329   was used to obtain the optimal fitted result. A constrained of $\sum f_{i,inorganics} + \sum f_{i,organics} = 1$ is used.

330   The modeled MFR is strongly dependent on the values of vaporization enthalpy (ΔH_{vap}) and

331   mass accommodation coefficient (α) (Lee et al., 2010;Lee et al., 2011). Thus, a sensitivity test is

332   performed to determine the ΔH_{vap} of OA and α based on the campaign average data (Fig. S4). A

333   linear relationship was adopted between ΔH_{vap} and $log_{10}C_i^*(T_{ref})$, $\Delta H_{vap} = -a \cdot$

334    $log_{10} C_i^*(T_{ref}) + b$, where a and b are fitting parameters (Epstein et al., 2010). The a and b values

335   are set to be [0, 4, 8, 12] and [50, 80, 100, 150, 200] in the sensitivity test, respectively, along with

336   α = [0.01, 0.09, 0.1, 0.5, 0.7, 0.9, 1]. The results show that the measured MFR was reproduced well

337   (with the lowest SSR of 0.0205, Fig. S5) by using ΔH_{vap}=80 kJ mol^{-1} with α of 0.09, 0.1 and 0.7,

338   respectively. For simplicity, ΔH_{vap}=80 kJ mol^{-1} and α=0.09 are considered as the best estimation

339   and adopted in the simulation of the whole campaign datasets. The extracted α value was consistent

340   with the values ($\alpha \leq 0.1$) reported previously (Saha et al., 2015; Park et al., 2013; Saleh et al., 2008;

341   Cappa and Jimenez, 2010), indicating significant resistance to mass transfer during evaporation. In

342   addition, the ΔH_{vap} of OA is of the same magnitude (80-150 kJ mol^{-1}) as reported in the literature

343   (Hong et al., 2017; Saha et al., 2017; Riipinen et al., 2010).

344   Note that the decomposition of particles during the heating process is ignored in the model.

345   Kiyoura and Urano (1970) suggested that ammonium sulfate would decompose to ammonium

346   bisulfate (NH_4HSO_4) or triammonium hydrogen sulfate ($(NH_4)_3H(SO_4)_2$), and ammonia (NH_3) when

347   heated to around 160-180 °C. Wang and Hildebrandt Ruiz (2018) also observed thermal

348   decomposition of organics and ammonium sulfate during evaporation by using a Filter Inlet for

349   Gases and AEROsols chemical-ionization mass spectrometer (FIGAERO-CIMS). It suggests that,

350   besides sublimation, decomposition might occur during evaporation of particles. However, the

351   mechanisms of decomposition are complex and remain unclear, which is difficult to simulate in our

352   model. We roughly estimated uncertainty caused by the decomposition and found that ignoring the

353   decomposition of organics would lead to an underestimation of SVOA, while the decomposition of

354    $(NH_4)_2SO_4$ played a minor role in the simulation (Sect. S2). However, the exact effects are still

355   highly uncertain. We hence exclude the decomposition of particles from the model for simplicity.

356   **3   Results and discussion**

357   **3.1 Overview**

358   Figure 1 shows the temporal profile of PNSD (a), aerosol chemical composition and total mass

359   concentration of $PM_{2.5}$ (b), mass fraction of each component (c), and wind speed and direction (d)

360   during the measurements. Note that the SP-AMS measurement started on 12th October. According

361   to the PNSD data, a total number of 20 new particle formation (NPF) events were observed during

362   the whole campaign. The background particles mainly exhibited unimodal distribution which

363   peaked at a size range of about 80-150 nm. The average particle number concentration (N_{CN}) in the

364   size range of 3-1000 nm was about 12700 cm^{-3}, much lower than that from the rural measurement

365   (18150 cm^{-3}) in 2006 in the PRD region (Rose et al., 2010). A wide accumulation mode was

366   observed during the period prevalent with north wind direction, implying that the air mass from the

367   north could bring pollutants from the city cluster around Guangzhou to the measurement site.

368   The chemical composition and the corresponding mass fraction measured by the SP-AMS (Fig.

369   1 b and c) were consistent with those of PNSD, which showed a significantly high mass

370   concentration of organics when the wind was from the north. The average mass fraction of PM_1 was

371   dominated by organics (51.8%), followed by sulfate (17.5%), nitrate (10.2%), BC (9.9%),

372   ammonium (8.8%), and chloride (1.7%). The mass concentration of organics varied from 3.3 to

373   123.4 μg m^{-3}, with an average value of 20.3 μg m^{-3}, lower than the value (25.7 μg m^{-3}) reported in

374   Guangzhou city (Qin et al., 2017), but significantly higher than that was observed (4.1 μg m^{-3}) in

375   Hong Kong (Lee et al., 2013). The mass distribution of the chemical species at the Heshan site was

376   similar to that measured in inland China (Chen et al., 2015; Huang et al., 2014), which was

377   dominated by organics from anthropogenic emissions. A distinguished and reproducible diurnal

378   pattern of the mass fraction was observed during the measurement (Fig. 1c), implying that the

379   particle composition was more affected by local emission or photochemical production than other

380   pathways. Organics showed a diurnal pattern with bimodal peaks respectively in the afternoon and

381   evening, which will be discussed later in section 3.3. The temporal profile of GF-PDF (Fig. 2)

382   measured by the H/V-TDMA was consistent with that of chemical composition, which showed a

383   significant diurnal pattern. This suggested that particles at all diameters could be affected by

384   atmospheric chemical processes and local emissions, which will be further discussed in section 3.3.

385   The H/V-TDMA data from 18th to 26th October and 29th October to 3rd November were not available

386   due to instrumental failure. In general, the GF-PDF exhibited a bimodal distribution for particles

387   larger than 30 nm, with a significant more-hygroscopic (MH, GF>1.33) or less-hygroscopic (LH,

388   1.11<GF<1.33) mode and a less obvious non-hygroscopic (NH, GF<1.11), indicating that these

389   particles were partly externally mixed. The NH mode with primary emissions (e.g., fresh black

390 carbon and some organics) was more obvious in a size range of 50-150 nm than others, suggesting

391 that these particles were more affected by local anthropogenic emissions. The above observation

392 was supported by the size distribution of the BC mass faction (Fig. S6), which peaked at a size range

393 of about 50-150 nm. Besides, the MH mode shifted to a higher GF value with an increase of particle

394 sizes, implying that larger particles were more aged with a higher fraction of inorganic salt (Fig. S6)

395 and well separated from the freshly emitted counterparts. A similar phenomenal pattern was

396 previously observed in the urban environment, including the PRD region (Hong et al., 2018; Cai et

397 al., 2017; Jiang et al., 2016; Tan et al., 2013b), the North China Plain (Liu et al., 2011; Ma et al.,

398 2016) and other city regions around the world (Yuan et al., 2020; Mochida et al., 2006; Massling et

399 al., 2005).

400 Table 3 summaries the N_{CCN}, activation ratio (AR), D_{50}, and κ_{CCN} values at 0.1%, 0.2%, 0.4%,

401 0.7%, 0.9%, and 1.0% SS during the campaign. The activation ratio is defined as the ratio of N_{CCN}

402 to N_{CN}, that is, $AR = N_{CCN}/N_{CN}$. The average N_{CCN} at 0.1%, 0.2%, 0.4%, 0.7%, 0.9%, and 1.0% SS

403 was about 2507, 4322, 5854, 6834, 7497, and 7862 cm^{-3}, respectively. The N_{CCN} at 0.7% SS was

404 lower than that measured (7900 cm^{-3} at 0.7% SS) in urban Guangzhou (Cai et al., 2018) and at a

405 suburban site (14400 cm^{-3} at 0.864% SS) in the North China Plain (Zhang et al., 2020), but

406 significantly higher than that measured at an urban site (2776 cm^{-3} at 0.68% SS) in São Paulo, Brazil

407 (Almeida et al., 2014). The average AR at the above six SS was 0.20, 0.34, 0.45, 0.52, 0.57, and

408 0.60, respectively. The AR at 0.7% SS was lower than the measured value (0.64 at 0.7% SS) in the

409 urban Guangzhou (Cai et al., 2018), while the corresponding D_{50} (52.56 nm) was lower than that

410 (58.45 nm) in the Guangzhou campaign, implying a higher CCN activity at this site. Thus, the lower

411 AR in this autumn campaign suggested that particles were more centered at smaller sizes, which

might be attributed to frequently occurred NPF at the Heshan site. The average κ values obtained

using HTDMA fall in a range of 0.1-0.17 at 30-200 nm (Fig. S7a), which were possibly attributed

to a high fraction of organic matter (Fig. S6). The κ_{AMS} is slightly higher than the κ_{HTDMA} and the

differences become larger with decreasing particle sizes. This was probably due to the overestimated

κ_{OA} at a small size range, which will be discussed in the next section. The hygroscopicity parameter

κ values obtained by the CCNc method were 0.48, 0.47, 0.31, 0.22, 0.20, and 0.20 at the above SS,

respectively, which were much higher than those measured by the HTDMA in this study. This

significant discrepancy between the measured κ_{CCN} and κ_{HTDMA} values might suggest that the water

uptake behavior is different under super- and sub-saturation condition, which is likely attributed to

the surfactant effect. It was reported that organic matter in the particles could serve as surfactant and

lower surface tension by about 0.01-0.032 N m^{-1}, leading to a higher CCN activity and thus a higher

κ_{CCN} (Petters and Kreidenweis, 2013; Ovadnevaite et al., 2017; Liu et al., 2018). According to Eqs.

(4) and (5), the κ_{CCN} was more susceptibly affected by the value of surface tension than that of

κ_{HTDMA}, which would lead to the discrepancy between κ_{CCN} and κ_{HTDMA} values. The surfactant effect

is closely related to the presence of liquid-liquid phase separation (LLPS) for organic-containing

particles at high RH (Renbaum-Wolff et al., 2016; Ruehl and Wilson, 2014). Once LLPS occurred,

the organic film on the droplet surface would decrease surface tension and enhance water uptake.

For particles of organic/inorganic mixture, the LLPS can occur when the O:C is lower than 0.8

(Bertram et al., 2011; Song et al., 2012a, b; Schill and Tolbert, 2013). The average O:C obtained

using AMS is about 0.53 in this campaign, suggesting that the LLPS likely occurred at

supersaturation conditions. Meanwhile, the variation of the discrepancy between κ_{CCN} and κ_{HTDMA}

is statistically insignificant during clean and polluted periods (Fig. S7b and c), implying that the

434 surfactant effect was hardly affected by pollution condition. Note that surface tension effect is not

435 the only factor which leads to a higher κ_{CCN}. It was found that κ_{CCN} could be higher than κ_{HTDMA},

436 since the existence of the slightly soluble compounds inhibits water uptake under subsaturation

437 conditions (Zhao et al., 2016; Pajunoja et al., 2015; Dusek et al., 2011; Petters et al., 2009; Hong et

438 al., 2014; Hansen et al., 2015). Other factors, such as different parameters used in the CCNc and

439 HTMDA calibration and function groups associated with the carbon chain, can lead to a gap between

440 κ_{HTDMA} and κ_{CCN} (Rose et al., 2008; Wex et al., 2009). More future work is needed to better

441 understand this water uptake mechanism and to improve the prediction of aerosol-cloud-climate

442 interactions.

443 **3.2 The average size-resolved hygroscopicity and volatility of OA**

444   The composition of organics could vary on a large scale with diameters due to different sources

445 and aging processes, which would further affect their properties. Figure 3 presents the average size-

446 resolved hygroscopicity and volatility of OA. The κ_{OA} values (vertical red lines in Fig. 3) ranged

447 from 0.058 to 0.09, within the range (0.05-0.15 at 100 nm) previously reported in the PRD region

448 (Hong et al., 2018) and slightly higher than that (0.03-0.06 at 250 nm) at a mountain site in Germany

449 (Wu et al., 2013). In general, the κ_{OA} values increased with particle sizes from 0.058 at 30 nm to

450 0.09 at 150 and 200 nm, similar to the feature observed in urban and forest environments (Kim et

451 al., 2020; Deng et al., 2019). The increases of the κ_{OA} values with particle sizes could be explained

452 by the oxidation level of organic aerosols (Massoli et al., 2010; Lambe et al., 2011; Xu et al., 2021).

453 Specifically, the hygroscopicity of OA was often found to be positively correlated to its oxidation

454 level (Mei et al., 2013; Lambe et al., 2011), which was usually represented by f_{44}, O/C ratio, or $\overline{OS_c}$.

455 Thus, the higher κ_{OA} values at larger particle diameters in this study might correspond to a higher

456 aging degree of these particles, and this was confirmed by the increasing trend of f_{44} with particle

457 diameters, i.e., the increasing fraction of CO_2^+ in OA in large particles (Fig. S8). Previous field

458 studies also indicated that f_{44} increased with particle diameters (Kim et al., 2020; Cai et al., 2018),

459 leading to a higher κ_{OA} value.

460   Besides the hygroscopicity of OA, we observed the size dependence of volatility. As shown in

461 Fig. 3, the mass fraction of ELVOA increases from 0.16 to 0.30 with the particle diameter, indicating

462 that the particles could be more aged at larger diameters, consistent with the higher κ_{OA} values as

463 discussed above. The ELVOA fraction in this campaign was higher than that in Beijing in summer

464 (0.13) measured by a thermodenuder (TD) coupled to an AMS (Xu et al., 2019), but similar to that

465 in Athens (0.3) using a similar TD system (Louvaris et al., 2017). The SVOA generally contributed

466 42%-57% to the OA at all measured sizes, comparable to the values reported in Centreville and

467 Raleigh (66-75%, Saha et al., 2017), Beijing (64%, Xu et al., 2019) and Mexico City (39%-73%,

468 Cappa and Jimenez, 2010). Note that the relationship between volatility and oxidation state of OA

469 is not usually strong. Saha et al. (2017) reported weak correlations (R < 0.3) between the mean

470 volatility ($\overline{C^*}$) and the mean oxidation state ($\overline{OS_C}$). Hong et al. (2017) also found that the volatility

471 distribution of OA derived from the combined V-TDMA and evaporation dynamic model could not

472 be fully explained by the organic factions determined by the PMF analysis based on the AMS data.

473 This is probably because the volatility was not only dependent on the $\overline{OS_C}$, but also the number of

474 atomic carbon (Donahue et al., 2011). In spite of this, the size-resolved volatility distribution can

475 provide a rough estimate of the aging degree of OA.

3.3 The diurnal variation of OA hygroscopicity and volatility

As discussed in Sect. 3.2, the hygroscopicity and volatility of OA could vary on a large range with particle diameters, which might be attributed to photochemical reactions and the OA sources. In this section, the diurnal variation of hygroscopicity and volatility of OA at different particle sizes was investigated, in combination with the PMF results. In general, the mass fraction of organics showed an obvious diurnal pattern during the whole campaign, with two peaks at about 14:00 and 19:00 LT (Fig. 4a), implying significant impacts of photochemical reactions and local emissions. Based on the PMF results (Fig. 5), the afternoon peak was attributed to secondary organics aerosol (SOA) formation (aBBOA and LOOA) during daytime, while the evening peak was explained by local residential activity (e.g., biomass burning and cooking, HOA and BBOA), as will be discussed later. A similar late-afternoon peak was observed in Hong Kong (Lee et al., 2013), where the OA enhancement was mainly contributed by traffic emissions. The f_{44} remained at a high level during daytime, consistent with strong photochemical reactions. A similar diurnal pattern was observed in the urban and sub-urban regions (Hong et al., 2018; Hu et al., 2016; Thalman et al., 2017), suggesting the consistent aging processes of pre-existing OA. In contrast, Deng et al. (2019) reported a relative low OA oxidation state during daytime in a forest environment, which could be explained by the SOA formation through photochemical oxidation of BVOCs.

The calculated κ_{HTDMA} and κ_{AMS} (the blue and red lines in Fig. 4b, respectively) values at 200 nm based on Eqs. (4) and (7) both reached minimum during daytime which was consistent with high OA fractions. This may be explained by lower hygroscopic of OA than inorganics as found in previous studies (Pajunoja et al., 2015; Zhao et al., 2015; Kuang et al., 2020b) as well as the low κ_i

497 values shown in Table 1. Although OA in a higher oxidation state could be hydrophilic (Massoli et

498 al., 2010), the primary OA is usually considered to be hydrophobic substance and their mixture

499 would be less hygroscopic (usually with average κ =0.1). The κ_{AMS} values were generally consistent

500 with those of the κ_{HTDMA} during daytime while the overestimated κ_{OA} was observed during nighttime.

501 This implies a lower κ_{OA} value than 0.1 at 200 nm during the nighttime, probably due to less

502 oxidation processes at night than those under the sunlight.

503   The average diurnal profile of PNSD is shown in Fig. 4c. Besides a stable accumulation mode

504 peaked at around 100 nm, a significantly growing mode of particle number from 20nm to 80 nm

505 was observed from 12:00 to 20:00 LT, which could be attributed to the frequently occurred NPF

506 during the campaign (Fig. 1a).

507   The size-resolved diurnal variations of κ_{OA} was explored in Fig. 6. Note that the κ_{OA} values are

508 presented in 2-hour resolution due to the low data coverage (Figs. 1 and 2). In general, a significantly

509 different pattern was observed between the Aitken mode and the accumulation mode. For Aitken

510 mode particles (30-100 nm), the κ_{OA} values were higher (0.05-0.1) before dawn than those (0.02-

511 0.07) during daytime, while this trend began to overturn at 150 and 200 nm, where the κ_{OA} values

512 peaked at noon (~0.09, Fig. 6). As reported in literature, the hygroscopicity of organics was partly

513 dependent on the aging degree (Liu et al., 2021; Zhao et al., 2016; Kim et al., 2020). The diurnal

514 characteristics of the size-resolved κ_{OA} indicate that the OA in small particles (30-100 nm) was fresh

515 and became aged in large particles. For the same campaign, Kuang et al. (2021) reported the bulk

516 κ_{OA} of PM_1 based on aerosol optical hygroscopicity measurements, which could provide high time

517 resolution data of κ_{OA}. The relationship between κ_{OA} and different OA factors was investigated,

518 which showed a negative correlation (R=-0.25) between LOOA and κ_{OA}, while a positive correlation

519 (R=0.35) between aBBOA and κ_{OA}. Thus, the decrease of κ_{OA} for Aitken mode particles during

520 daytime might be attributed to the daytime formation of LOOA through gas-particle partitioning

521 (Fig. 5). A similar phenomenon was reported by Deng et al. (2019) in a forest environment, which

522 might be attributed to the photochemical reactions of BVOCs. Therefore, OA in small particles

523 might be less aged and was primarily contributed by photochemical oxidation of VOCs. In contrast,

524 it is likely that the accumulation mode particles became aged through photochemical oxidation

525 during daylight, as evidenced by higher fractions of ELVOA at 200 nm and higher κ_{OA} (Figs. 6 and

526 7) during daytime. According to the PMF analysis, the daytime formation of aBBOA likely resulted

527 from the aging processes of primary OA or biomass burning related precursors (Fig. 5). As suggested

528 by Kuang et al. (2021), the daytime formation of aBBOA (Fig. 5) would lead to an increase of κ_{OA},

529 which likely explained the noontime κ_{OA} peak at 150 and 200 nm. It suggested that the OA in the

530 accumulation mode was more influenced by the aging processes through photochemical reactions

531 (leading to aBBOA formation).

532   The average size-resolved volatility distribution of OA during daytime (8:00 to 16:00 LT) and

533 nighttime (20:00 to 4:00 LT) was demonstrated in Fig. 7. A higher fraction of semi-volatile organic

534 aerosol (SVOA) was observed at six measured sizes (30, 50, 80, 100, 150, and 200 nm) during

535 daytime. SVOA was usually related to primary emission (e.g., traffic, biomass burning) and gas-

536 particle partitioning (Donahue et al., 2012;Jathar et al., 2020;Hong et al., 2017; Saha et al., 2017).

537 Two primary emission factors, BBOA and HOA, remained at a relative low level during daytime,

538 suggesting that the higher fraction of SVOA during daylight might be more originated from gas-

539 particle partitioning. Note that gas-particle partitioning (leading to LOOA formation) could occur

540 at all measured diameters, as shown by the higher daytime fractions of SVOA (Fig. 7). In summary,

541   the above results indicate that the negative effect of LOOA on κ_{OA} might exist at all diameters, while

542   the positive effect of aBBOA was more dominant at larger particle sizes.

543   Meanwhile, the decreasing trend of κ_{OA} was observed from 18:00 to 24:00 at 80 and 100 nm

544   which might be related to the high mass fraction of OA from primary emissions (HOA and BBOA,

545   Fig. 5), owing to their hydrophobic nature. These two primary factors were associated with traffic

546   emissions, cooking and biomass burning. Zhang et al. (2005b) constructed the size distribution of

547   HOA based on the size-resolved m/z 44 and 57 from the AMS measurement and showed that HOA

548   was dominant ($\sim$75%) in ultrafine particles (D_{va}<100 nm). The size-resolved PMF results from Sun

549   et al. (2012) also indicated a high mass fraction of HOA (0.3-0.4) in Aitken mode particles. The

550   mass distribution of BC could be used to represent the distribution of primary OA (Cubison et al.,

551   2008;Wang et al., 2010;Zhang et al., 2005a) due to similar source origins for BC and HOA/BBOA.

552   The average mass fraction of BC peaked at about 80-100 nm (Fig. S6a), suggesting that HOA and

553   BBOA might be dominant at this size range. The BC peaks at 80 nm and 100 nm were consistent

554   with those of the SVOA mass fraction (Fig. 3), which was attributed to biomass burning as similar

555   characteristics for the BC peak were shown in other studies (May et al., 2013;Huffman et al.,

556   2009;Donahue et al., 2011). Furthermore, this conclusion was supported by the hygroscopicity

557   measurements as a significant NH mode for 80-100 nm particles was found (Fig. 2). Overall, these

558   results highlight that the diurnal variation of physicochemical properties of OA could vary in a large

559   range with particle diameters, and further investigation is needed.

560   **3.4 Implication for CCN activity**

561   The CCN activity and its prediction is essential in global climate model and evaluation. A κ_{OA}

562 value of 0.1~0.15 was widely adopted in the prediction of N_{CCN} based on aerosol chemical

563 composition (Meng et al., 2014; Wang et al., 2010; Almeida et al., 2014). As discussed in Sect. 3.3,

564 the κ_{OA} values might be dependent on particle sizes and vary diurnally, which in turn affect N_{CCN}.

565 Here, different κ_{OA} values were adopted to predict N_{CCN} and the impact of κ_{OA} on N_{CCN} was

566 investigated through comparison between the predicted and measured N_{CCN}. Note that we only

567 discussed the N_{CCN} at 0.1%, 0.2%, 0.4% and 0.7% SS, since the D_{50} at higher SS (0.9% and 1.0%)

568 was within a narrow range (35-60 nm).

569   The N_{CCN} at a certain SS can be calculated using PNSD and D_{50}:

570 $$N_{CCN,p}(SS) = \int_{D_{50}}^{\infty} n_i \, dlogDp_i \tag{16}$$

571 where n_i is the particle distribution function at Dp_i and D_{50} is determined from the κ_{AMS} using Eqs.

572 (5) and (7). The D_{50} at 0.1%, 0.2%, 0.4% and 0.7% SS ranged from about 130-160 nm, 90-110 nm,

573 60-80 nm and 45-60 nm, respectively. Three κ_{OA} schemes were proposed to predict N_{CCN}: (1) fixed

574 κ_{OA}, where κ_{OA} was assumed to be 0.1 for all size particles. (2) size-resolved κ_{OA} (SR κ_{OA}), where

575 κ_{OA} was taken from average size-resolved κ_{OA} (κ_{OA} at 50, 80, 100 and 150 nm for 0.7%, 0.4%, 0.2%

576 and 0.1% SS, respectively) in Sect. 3.2. (3) size-resolved diurnal κ_{OA} (SR diurnal κ_{OA}), where κ_{OA}

577 was the average diurnal value of κ_{OA} at each diameter (κ_{OA} at 50, 80, 100 and 150 nm for 0.7%,

578 0.4%, 0.2% and 0.1% SS, respectively) as shown in Sect. 3.3. The κ_{AMS} was calculated based on the

579 chemical composition at the corresponding D_{50} range. Note that the N_{CCN} prediction based on the

580 SR diurnal κ_{OA} scheme was presented in 2 h time resolution and the particles were assumed to be

581 internally mixed in Eq. (16). The internal mixing assumption could slightly increase the predicted

582 N_{CCN} by about 6-10% (Sect. S3). As aforementioned, organics can increase the CCN activity by

583 decreasing surface tension, which might lead to significant discrepancy between κ_{HTDMA} and κ_{CCN}

584   in this campaign (Fig. S7). In addition, this effect could result in a significant underestimation of

585   N_{CCN} (Ovadnevaite et al., 2017; Liu et al., 2018; Good et al., 2010; Noziere, 2016).

586   Here, we evaluate the surface tension effect by comparing κ_{HTDMA} and κ_{CCN} as a function of

587    $\sigma_{s/a}$ (Fig. S9). The κ_{CCN} reached κ_{HTDMA} when the $\sigma_{s/a}$ values were set to be about 0.059 N m^{-1} at

588   0.7%, 0.9% and 1.0% SS, 0.053 N m^{-1} at 0.4% SS, 0.047 N m^{-1} at 0.2% SS, and 0.049 N m^{-1} at 0.1%

589   SS, respectively. Thus, we adopted $\sigma_{s/a}$ values of 0.049, 0.047, 0.053 and 0.059 N m^{-1} to predict

590   N_{CCN} at 0.1%, 0.2%, 0.4% and 0.7% SS, respectively. In general, the N_{CCN} prediction could be

591   significantly improved by considering the surfactant effect (Fig. S10). The N_{CCN} was slightly

592   overestimated by using reduced $\sigma_{s/a}$ values, which was probably due to using a fixed κ_{OA} values.

593   This bias could be corrected by adopting SR κ_{OA} scheme (Fig. S11).

594   The deviation of the N_{CCN} prediction ($\delta_{N_{CCN}}$) at a certain SS is defined as (Cai et al., 2021b):

595    $$\delta_{N_{CCN}}(SS) = \frac{N_{CCN,m}(SS) - N_{CCN,p}(SS)}{N_{CCN,m}(SS)} 100\% \qquad\qquad (17)$$

596   where $N_{CCN,m}(SS)$ is the measured N_{CCN} at a specific SS. A negative $\delta_{N_{CCN}}$ indicates an

597   overestimate of N_{CCN}, and vice versa.

598   Figure 8 shows the $\delta_{N_{CCN}}$ at different SS for the three κ_{OA} schemes. Fixed κ_{OA} scheme gave

599   generally a negative value of $\delta_{N_{CCN}}$ (-0.18 to -0.02) at 0.7% SS, indicating an N_{CCN} overestimation,

600   due to lower κ_{OA} values for smaller particles. A significant diurnal pattern of $\delta_{N_{CCN}}$ was observed at

601   all SS. The $\delta_{N_{CCN}}$ was relatively higher during daytime at 0.1% SS, while an opposite pattern was

602   shown at high SS, consistent with the size-dependent variation of κ_{OA} (Fig. 6). Hence, the fixed κ_{OA}

603   scheme could lead to an obvious discrepancy in the N_{CCN} prediction as SS increased. The results

604   based on the SR κ_{OA} scheme showed that the minimum $\delta_{N_{CCN}}$ value at 0.7% SS increased from -

605   0.18 in the fixed κ_{OA} scheme to -0.08, indicating the improvement for the N_{CCN} prediction at high

606   SS (Fig. 8b). However, only minor improvement was observed at SS lower than 0.4 % because of

607   the low employed κ_{OA} (about 0.08), which was close to the κ_{OA} value (0.1) adopted in the fixed κ_{OA}

608   scheme. A significant difference of $\delta_{N_{CCN}}$ was still observed in the diurnal pattern at high and low

609   SS, implying the impact of the diurnal variation of κ_{OA} on the N_{CCN} prediction. To further investigate

610   this impact, the SR diurnal κ_{OA} scheme was employed to calculate $\delta_{N_{CCN}}$ and the results were shown

611   in Fig. 8c. The $\delta_{N_{CCN}}$ value at 0.7% SS varied from -0.04 to 0.09 with an average value of 0, whereas

612   it ranged from 0 to 0.11 at 0.1% SS. Hence, the discrepancies of $\delta_{N_{CCN}}$ among different SS became

613   minor compared to the other two schemes as a relatively flat diurnal pattern of $\delta_{N_{CCN}}$ was observed

614   at all SS. It implies that better prediction of N_{CCN} could be achieved by considering the diurnal

615   variation and the size dependence of κ_{OA}.

616   **4.   Conclusions**

617   A rural field measurement was conducted at the Heshan supersite in the PRD region of China

618   during October and November 2019. We investigated the diurnal variation and size dependence in

619   the hygroscopicity and volatility of OA in combination with the PMF analysis of the AMS data. The

620   impacts of OA on the CCN number concentration at different SS were discussed for various given

621   size-dependent κ_{OA} values.

622   In general, the average κ_{OA} values varied from 0.058 at 30 nm to 0.09 at 200 nm, indicating a

623   higher oxidation degree of OA at larger sizes than at smaller sizes. This is consistent with particle

624   volatility: the mass fraction of ELVOA increased (0.16-0.30) with increasing particle diameters.

625   Our results suggest that the formation and aging processes of OA might vary with particle sizes.

626 An oppositely diurnal pattern of κ_{OA} was observed between Aitken mode (30-100 nm) and

627 Accumulation mode (150 and 200 nm) particles, suggesting different atmospheric evolution

628 processes of OA at different diameters. The gas-particle partitioning could decrease the κ_{OA}, while

629 the aging processes of preexisting particles could enhance the hygroscopicity of OA. For Aitken

630 mode particles (30-100 nm), the κ_{OA} values reached minimal (0.02-0.07) during daytime.

631 Meanwhile, a daytime peak was observed for the κ_{OA} value (~0.09) in the accumulation mode (150

632 and 200 nm), suggesting that the aging processes of preexisting particles were more dominant at

633 accumulation mode particles. In addition, the mass faction of SVOA was higher during daytime at

634 all measured diameters, implying that the formation of LOOA through gas-particle partitioning was

635 independent of particle diameters.

636 The impact of the size-resolved diurnal variation of κ_{OA} on the N_{CCN} was investigated. The use

637 of fixed κ_{OA} (κ_{OA}=0.1) overestimated the N_{CCN} up to 18% at 0.7% SS. The diurnal deviation became

638 obvious at 0.7% SS and minor at 0.1% SS during daytime, owing to the size-dependent variation of

639 κ_{OA}. The N_{CCN} prediction at 0.7% SS was improved if the SR κ_{OA} scheme was used, while the

640 diurnal variation of $\delta_{N_{CCN}}$ still existed. Better predictions can be obtained by using SR diurnal κ_{OA}.

641 Our results highlight that the physical properties of OA can vary in a large range at different size

642 ranges due to the formation and aging processes, and the size-resolved diurnal variation in κ_{OA} plays

643 an important role in the N_{CCN} prediction at different SS. Further studies on the size-resolved

644 physicochemical properties of OA should be performed in different environments to better

645 understand their impact on cloud formation and hence climate.

646

647 *Data availability.* Data from the measurements are available at

648   https://doi.org/10.6084/m9.figshare.18094277.v1 (Cai et al., 2022).

649

650   *Supplement.* The supplement related to this article is available online at xxx.

651

652   *Author contributions.* **MC, SH, BY and LL** designed the research. **MC**, **SH, MS, BY, YP, ZW, DC,**

653   **WC, QS, WL, BL and QS** performed the measurements. **MC, SH, BL, QS, LL, BY, WH, WC,**

654   **QS, WL, YP, ZW, HT, HX, FL, DX, TD, JS and JZ** analyzed the data. **MC, SH** and **LL** wrote the

655   paper with contributions from all co-authors.

656

657   *Competing interests.* The authors declare that they have no conflict of interest.

658

659   *Financial support.* This work was supported by the National Key R&D Plan of China (grant no.

660   2019YFC0214605, 2019YFE0106300, and 2018YFC0213904), the Key-Area Research and

661   Development Program of Guangdong Province (grant no. 2019B110206001), the National Natural

662   Science Foundation of China (grant nos. 41877302, 91644225, 41775117 and 41807302),

663   Guangdong Natural Science Funds for Distinguished Young Scholar (grant no. 2018B030306037),

664   Guangdong Innovative and Entrepreneurial Research Team Program (grant no. 2016ZT06N263),

665   Guangdong Province Key Laboratory for Climate Change and Natural Disaster Studies (grant no.

666   2020B1212060025), Guangdong Basic and Applied Basic Research Foundation (grant nos.

667   2019A1515110790 and 2019A1515110791), Science and Technology Research project of

668   Guangdong Meteorological Bureau (grant no. GRMC2018M07), the Natural Science Foundation of

669   Guangdong Province, China (grant no. 2016A030311007), Science and Technology Innovation

670   Team Plan of Guangdong Meteorological Bureau (grant no. GRMCTD202003), and Science and

671   Technology Program of Guangdong Province (Science and Technology Innovation Platform

672   Category, No. 2019B121201002).

673

674   *Acknowledgements.* Additional support from the crew of the Heshan supersite and Guangdong

675   Environmental Monitoring Center is greatly acknowledged.

676

References

678   Almeida, G. P., Brito, J., Morales, C. A., Andrade, M. F., and Artaxo, P.: Measured and

679   modelled cloud condensation nuclei (CCN) concentration in São Paulo, Brazil: the importance of

680   aerosol size-resolved chemical composition on CCN concentration prediction, Atmos. Chem. Phys.,

681   14, 7559-7572, 10.5194/acp-14-7559-2014, 2014.

682   Bertram, A. K., Martin, S. T., Hanna, S. J., Smith, M. L., Bodsworth, A., Chen, Q., Kuwata, M., Liu,

683   A., You, Y., and Zorn, S. R.: Predicting the relative humidities of liquid-liquid phase separation,

684   efflorescence, and deliquescence of mixed particles of ammonium sulfate, organic material, and water

685   using the organic-to-sulfate mass ratio of the particle and the oxygen-to-carbon elemental ratio of the

686   organic component, Atmos. Chem. Phys., 11, 10995-11006, 10.5194/acp-11-10995-2011, 2011.

687   Cai, J., Chu, B., Yao, L., Yan, C., Heikkinen, L. M., Zheng, F., Li, C., Fan, X., Zhang, S., Yang,

688   D., Wang, Y., Kokkonen, T. V., Chan, T., Zhou, Y., Dada, L., Liu, Y., He, H., Paasonen, P., Kujansuu,

689   J. T., Petäjä, T., Mohr, C., Kangasluoma, J., Bianchi, F., Sun, Y., Croteau, P. L., Worsnop, D. R.,

690   Kerminen, V. M., Du, W., Kulmala, M., and Daellenbach, K. R.: Size-segregated particle number

691   and mass concentrations from different emission sources in urban Beijing, Atmos. Chem. Phys., 20,

692   12721-12740, 10.5194/acp-20-12721-2020, 2020.

693   Cai, M., Huang, S., Li, L., Yuan, B., Shao, M., and Zhao, J.: Distinct size dependence and

694   diurnal variation of OA hygroscopicity, volatility, and CCN activity at a rural site in the Pearl River

695   Delta (PRD) region, China. figshare. Dataset., https://doi.org/10.6084/m9.figshare.18094277.v1,

696   2022.

697   Cai, M., Tan, H., Chan, C. K., Mochida, M., Hatakeyama, S., Kondo, Y., Schurman, M. I., Xu,

698   H., Li, F., and Shimada, K.: Comparison of Aerosol Hygroscopcity, Volatility, and Chemical

699   Composition between a Suburban Site in the Pearl River Delta Region and a Marine Site in Okinawa,

700   Aerosol Air Qual. Res., 2017.

701   Cai, M., Tan, H., Chan, C. K., Qin, Y., Xu, H., Li, F., Schurman, M. I., Liu, L., and Zhao, J.:

702   The size-resolved cloud condensation nuclei (CCN) activity and its prediction based on aerosol

703   hygroscopicity and composition in the Pearl Delta River (PRD) region during wintertime 2014,

704   Atmos. Chem. Phys., 18, 16419-16437, 2018.

705   Cai, M., Liang, B., Sun, Q., Liu, L., Yuan, B., Shao, M., Huang, S., Peng, Y., Wang, Z., Tan,

706   H., Li, F., Xu, H., Chen, D., and Zhao, J.: The important roles of surface tension and growth rate in

707   the contribution of new particle formation (NPF) to cloud condensation nuclei (CCN) number

708   concentration: evidence from field measurements in southern China, Atmos. Chem. Phys., 21, 8575-

709   8592, 10.5194/acp-21-8575-2021, 2021a.

710   Cai, M. F., Liang, B. L., Sun, Q. B., Zhou, S. Z., Yuan, B., Shao, M., Tan, H. B., Xu, Y. S., Ren,

711   L. H., and Zhao, J.: Contribution of New Particle Formation to Cloud Condensation Nuclei Activity

712   and its Controlling Factors in a Mountain Region of Inland China, J. Geophys. Res. Atmos., 126,

713   e2020JD034302, https://doi.org/10.1029/2020JD034302, 2021b.

714   Canagaratna, M. R., Jayne, J. T., Jimenez, J. L., Allan, J. D., Alfarra, M. R., Zhang, Q., Onasch,

715   T. B., Drewnick, F., Coe, H., Middlebrook, A., Delia, A., Williams, L. R., Trimborn, A. M.,

716   Northway, M. J., DeCarlo, P. F., Kolb, C. E., Davidovits, P., and Worsnop, D. R.: Chemical and

717   microphysical characterization of ambient aerosols with the aerodyne aerosol mass spectrometer,

718   Mass Spectrom. Rev., 26, 185-222, 10.1002/mas.20115, 2007.

719   Cappa, C. D., and Jimenez, J. L.: Quantitative estimates of the volatility of ambient organic

720   aerosol, Atmos. Chem. Phys., 10, 5409-5424, 10.5194/acp-10-5409-2010, 2010.

721   Chang, R. Y. W., Slowik, J. G., Shantz, N. C., Vlasenko, A., Liggio, J., Sjostedt, S. J., Leaitch,

722   W. R., and Abbatt, J. P. D.: The hygroscopicity parameter (κ) of ambient organic aerosol at a field

723   site subject to biogenic and anthropogenic influences: relationship to degree of aerosol oxidation,

Atmos. Chem. Phys.,10,11(2010-06-01), 10, 5047-5064, 2010.

Chen, C., Sun, Y. L., Xu, W. Q., Du, W., Zhou, L. B., Han, T. T., Wang, Q. Q., Fu, P. Q., Wang, Z. F., Gao, Z. Q., Zhang, Q., and Worsnop, D. R.: Characteristics and sources of submicron aerosols above the urban canopy (260 m) in Beijing, China, during the 2014 APEC summit, Atmos. Chem. Phys., 15, 12879-12895, 10.5194/acp-15-12879-2015, 2015.

Chen, J., Budisulistiorini, S. H., Itoh, M., Lee, W. C., Miyakawa, T., Komazaki, Y., Yang, L. D. Q., and Kuwata, M.: Water uptake by fresh Indonesian peat burning particles is limited by water-soluble organic matter, Atmos. Chem. Phys., 17, 11591-11604, 10.5194/acp-17-11591-2017, 2017.

Cheung, H. H., Tan, H., Xu, H., Li, F., Wu, C., Yu, J. Z., and Chan, C. K.: Measurements of non-volatile aerosols with a VTDMA and their correlations with carbonaceous aerosols in Guangzhou, China, Atmos. Chem. Phys., 16, 8431-8446, 2016.

Cubison, M. J., Ervens, B., Feingold, G., Docherty, K. S., Ulbrich, I. M., Shields, L., Prather, K., Hering, S., and Jimenez, J. L.: The influence of chemical composition and mixing state of Los Angeles urban aerosol on CCN number and cloud properties, Atmos. Chem. Phys., 8, 5649-5667, 10.5194/acp-8-5649-2008, 2008.

Deng, Y., Kagami, S., Ogawa, S., Kawana, K., Nakayama, T., Kubodera, R., Adachi, K., Hussein, T., Miyazaki, Y., and Mochida, M.: Hygroscopicity of Organic Aerosols and Their Contributions to CCN Concentrations Over a Midlatitude Forest in Japan, J. Geophys. Res. Atmos., 123, 9703-9723, 10.1029/2017JD027292, 2018.

Deng, Y., Yai, H., Fujinari, H., Kawana, K., Nakayama, T., and Mochida, M.: Diurnal variation and size dependence of the hygroscopicity of organic aerosol at a forest site in Wakayama, Japan: their relationship to CCN concentrations, Atmos. Chem. Phys., 19, 5889-5903, 10.5194/acp-19-5889-2019, 2019.

Donahue, N. M., Epstein, S. A., Pandis, S. N., and Robinson, A. L.: A two-dimensional volatility basis set: 1. organic-aerosol mixing thermodynamics, Atmos. Chem. Phys., 11, 3303-3318, 10.5194/acp-11-3303-2011, 2011.

Donahue, N. M., Kroll, J. H., Pandis, S. N., and Robinson, A. L.: A two-dimensional volatility basis set – Part 2: Diagnostics of organic-aerosol evolution, Atmos. Chem. Phys., 12, 615-634, 10.5194/acp-12-615-2012, 2012.

753 Dusek, U., Frank, G. P., Massling, A., Zeromskiene, K., Iinuma, Y., Schmid, O., Helas, G.,

754 Hennig, T., Wiedensohler, A., and Andreae, M. O.: Water uptake by biomass burning aerosol at sub-

755 and supersaturated conditions: closure studies and implications for the role of organics, Atmos.

756 Chem. Phys., 11, 9519-9532, 10.5194/acp-11-9519-2011, 2011.

757 Engelhart, G. J., Moore, R. H., Nenes, A., and Pandis, S. N.: Cloud condensation nuclei activity

758 of isoprene secondary organic aerosol, J. Geophys. Res. Atmos., 116,

759 https://doi.org/10.1029/2010JD014706, 2011.

760 Epstein, S. A., Riipinen, I., and Donahue, N. M.: A Semiempirical Correlation between

761 Enthalpy of Vaporization and Saturation Concentration for Organic Aerosol, Environ. Sci. Technol.,

762 44, 743-748, 10.1021/es902497z, 2010.

763 Gantt, B., and Meskhidze, N.: The physical and chemical characteristics of marine primary

764 organic aerosol: a review, Atmos. Chem. Phys., 13, 3979-3996, 10.5194/acp-13-3979-2013, 2013.

765 Good, N., Topping, D., Allan, J., Flynn, M., Fuentes, E., Irwin, M., Williams, P., Coe, H., and

766 McFiggans, G.: Consistency between parameterisations of aerosol hygroscopicity and CCN activity

767 during the RHaMBLe discovery cruise, Atmos. Chem. Phys., 10, 3189-3203, 2010.

768 Guo, J., Zhou, S., Cai, M., Zhao, J., Song, W., Zhao, W., Hu, W., Sun, Y., He, Y., Yang, C., Xu,

769 X., Zhang, Z., Cheng, P., Fan, Q., Hang, J., Fan, S., Wang, X., and Wang, X.: Characterization of

770 submicron particles by time-of-flight aerosol chemical speciation monitor (ToF-ACSM) during

771 wintertime: aerosol composition, sources, and chemical processes in Guangzhou, China, Atmos.

772 Chem. Phys., 20, 7595-7615, 10.5194/acp-20-7595-2020, 2020.

773 Gysel, M., Crosier, J., Topping, D. O., Whitehead, J. D., Bower, K. N., Cubison, M. J., Williams,

774 P. I., Flynn, M. J., McFiggans, G. B., and Coe, H.: Closure study between chemical composition

775 and hygroscopic growth of aerosol particles during TORCH2, Atmos. Chem. Phys., 7, 6131-6144,

776 10.5194/acp-7-6131-2007, 2007.

777 Hallquist, M., Wenger, J. C., Baltensperger, U., Rudich, Y., Simpson, D., Claeys, M., Dommen,

778 J., Donahue, N., George, C., and Goldstein, A.: The formation, properties and impact of secondary

779 organic aerosol: current and emerging issues, Atmospheric chemistry and physics, 9, 5155-5236,

780 2009.

781 Hansen, A. M. K., Hong, J., Raatikainen, T., Kristensen, K., Ylisirniö, A., Virtanen, A., Petäjä, T.,

782   Glasius, M., and Prisle, N. L.: Hygroscopic properties and cloud condensation nuclei activation of

783   limonene-derived organosulfates and their mixtures with ammonium sulfate, Atmos. Chem. Phys., 15,

784   14071-14089, 10.5194/acp-15-14071-2015, 2015.

785   Hersey, S. P., Craven, J. S., Metcalf, A. R., Lin, J., Lathem, T., Suski, K. J., Cahill, J. F., Duong, H.

786   T., Sorooshian, A., Jonsson, H. H., Shiraiwa, M., Zuend, A., Nenes, A., Prather, K. A., Flagan, R. C., and

787   Seinfeld, J. H.: Composition and hygroscopicity of the Los Angeles Aerosol: CalNex, Journal of

788   Geophysical Research: Atmospheres, 118, 3016-3036, https://doi.org/10.1002/jgrd.50307, 2013.

789   Hong, J., Äijälä, M., Häme, S. A. K., Hao, L., Duplissy, J., Heikkinen, L. M., Nie, W., Mikkilä,

790   J., Kulmala, M., Prisle, N. L., Virtanen, A., Ehn, M., Paasonen, P., Worsnop, D. R., Riipinen, I.,

791   Petäjä, T., and Kerminen, V. M.: Estimates of the organic aerosol volatility in a boreal forest using

792   two independent methods, Atmos. Chem. Phys., 17, 4387-4399, 10.5194/acp-17-4387-2017, 2017.

793   Hong, J., Xu, H., Tan, H., Yin, C., Hao, L., Li, F., Cai, M., Deng, X., Wang, N., Su, H., Cheng,

794   Y., Wang, L., Petäjä, T., and Kerminen, V. M.: Mixing state and particle hygroscopicity of organic-

795   dominated aerosols over the Pearl River Delta region in China, Atmos. Chem. Phys., 18, 14079-

796   14094, 10.5194/acp-18-14079-2018, 2018.

797   Hong, J., Häkkinen, S. A. K., Paramonov, M., Äijälä, M., Hakala, J., Nieminen, T., Mikkilä, J.,

798   Prisle, N. L., Kulmala, M., Riipinen, I., Bilde, M., Kerminen, V. M., and Petäjä, T.: Hygroscopicity, CCN

799   and volatility properties of submicron atmospheric aerosol in a boreal forest environment during the

800   summer of 2010, Atmos. Chem. Phys., 14, 4733-4748, 10.5194/acp-14-4733-2014, 2014.Hu, W., Hu,

801   M., Hu, W., Jimenez, J. L., Yuan, B., Chen, W., Wang, M., Wu, Y., Chen, C., Wang, Z., Peng, J.,

802   Zeng, L., and Shao, M.: Chemical composition, sources, and aging process of submicron aerosols

803   in Beijing: Contrast between summer and winter, J. Geophys. Res. Atmos., 121, 1955-1977,

804   https://doi.org/10.1002/2015JD024020, 2016.

805   Huang, R.-J., Zhang, Y., Bozzetti, C., Ho, K.-F., Cao, J.-J., Han, Y., Daellenbach, K. R., Slowik,

806   J. G., Platt, S. M., and Canonaco, F.: High secondary aerosol contribution to particulate pollution

807   during haze events in China, Nature, 514, 218, 2014.

808   Huang, S., Wu, Z., Poulain, L., van Pinxteren, M., Merkel, M., Assmann, D., Herrmann, H.,

809   and Wiedensohler, A.: Source apportionment of the organic aerosol over the Atlantic Ocean from

810   53°N to 53°S: significant contributions from marine emissions and long-range transport, Atmos.

811   Chem. Phys., 18, 18043-18062, 10.5194/acp-18-18043-2018, 2018.

812   Huffman, J. A., Docherty, K. S., Aiken, A. C., Cubison, M. J., Ulbrich, I. M., DeCarlo, P. F.,

813   Sueper, D., Jayne, J. T., Worsnop, D. R., Ziemann, P. J., and Jimenez, J. L.: Chemically-resolved

814   aerosol volatility measurements from two megacity field studies, Atmos. Chem. Phys., 9, 7161-

815   7182, 10.5194/acp-9-7161-2009, 2009.

816   Jathar, S. H., Sharma, N., Galang, A., Vanderheyden, C., Takhar, M., Chan, A. W. H., Pierce, J.

817   R., and Volckens, J.: Measuring and modeling the primary organic aerosol volatility from a modern

818   non-road   diesel   engine,   Atmos.   Environ.,   223,   117221,

819   https://doi.org/10.1016/j.atmosenv.2019.117221, 2020.

820   Jiang, R., Tan, H., Tang, L., Cai, M., Yin, Y., Li, F., Liu, L., Xu, H., Chan, P. W., and Deng, X.:

821   Comparison of aerosol hygroscopicity and mixing state between winter and summer seasons in Pearl

822   River Delta region, China, Atmos. Res., 169, 160-170, 2016.

823   Jimenez, J. L., Canagaratna, M., Donahue, N., Prevot, A., Zhang, Q., Kroll, J. H., DeCarlo, P.

824   F., Allan, J. D., Coe, H., and Ng, N.: Evolution of organic aerosols in the atmosphere, Science, 326,

825   1525-1529, 2009.

826   Kanakidou, M., Seinfeld, J., Pandis, S., Barnes, I., Dentener, F., Facchini, M., Dingenen, R. V.,

827   Ervens, B., Nenes, A., and Nielsen, C.: Organic aerosol and global climate modelling: a review,

828   Atmos. Chem. Phys., 5, 1053-1123, 2005.

829   Kim, N., Yum, S. S., Park, M., Park, J. S., Shin, H. J., and Ahn, J. Y.: Hygroscopicity of urban

830   aerosols and its link to size-resolved chemical composition during spring and summer in Seoul,

831   Korea, Atmos. Chem. Phys., 20, 11245-11262, 10.5194/acp-20-11245-2020, 2020.

832   Kiyoura, R., and Urano, K.: Mechanism, Kinetics, and Equilibrium of Thermal Decomposition

833   of Ammonium Sulfate, Ind. Eng. Chem. Process Des. Dev. , 9, 489-494, 10.1021/i260036a001,

834   1970.

835   Kuang, Y., He, Y., Xu, W., Yuan, B., Zhang, G., Ma, Z., Wu, C., Wang, C., Wang, S., Zhang,

836   S., Tao, J., Ma, N., Su, H., Cheng, Y., Shao, M., and Sun, Y.: Photochemical Aqueous-Phase

837   Reactions Induce Rapid Daytime Formation of Oxygenated Organic Aerosol on the North China

838   Plain, Environ. Sci. Technol., 54, 3849-3860, 10.1021/acs.est.9b06836, 2020a.

839   Kuang, Y., Xu, W., Tao, J., Ma, N., Zhao, C., and Shao, M.: A Review on Laboratory Studies

840 and Field Measurements of Atmospheric Organic Aerosol Hygroscopicity and Its Parameterization

841 Based on Oxidation Levels, Curr. Pollut. Rep., 10.1007/s40726-020-00164-2, 2020b.

842 Kuang, Y., Huang, S., Xue, B., Luo, B., Song, Q., Chen, W., Hu, W., Li, W., Zhao, P., Cai, M.,

843 Peng, Y., Qi, J., Li, T., Wang, S., Chen, D., Yue, D., Yuan, B., and Shao, M.: Contrasting effects of

844 secondary organic aerosol formations on organic aerosol hygroscopicity, Atmos. Chem. Phys., 21,

845 10375-10391, 10.5194/acp-21-10375-2021, 2021.

846 Lambe, A. T., Onasch, T. B., Massoli, P., Croasdale, D. R., Wright, J. P., Ahern, A. T., Williams,

847 L. R., Worsnop, D. R., Brune, W. H., and Davidovits, P.: Laboratory studies of the chemical

848 composition and cloud condensation nuclei (CCN) activity of secondary organic aerosol (SOA) and

849 oxidized primary organic aerosol (OPOA), Atmos. Chem. Phys., 11, 8913-8928, 10.5194/acp-11-

850 8913-2011, 2011.

851 Lee, B.-H., Kostenidou, E., Hildebrandt, L., Riipinen, I., Engelhart, G., Mohr, C., DeCarlo, P.,

852 Mihalopoulos, N., Prevot, A., Baltensperger, U.: Measurement of the ambient organic aerosol

853 volatility distribution: application during the Finokalia Aerosol Measurement Experiment (FAME-

854 2008), Atmos. Chem. Phys., 10, 12149-12160, 2010.

855 Lee, B.-H., Pierce, J. R., Engelhart, G. J., and Pandis, S. N.: Volatility of secondary organic

856 aerosol from the ozonolysis of monoterpenes, Atmos. Environ., 45, 2443-2452, 2011.

857 Lee, B. P., Li, Y. J., Yu, J. Z., Louie, P. K., and Chan, C. K.: Physical and chemical

858 characterization of ambient aerosol by HR-ToF-AMS at a suburban site in Hong Kong during

859 springtime 2011, J. Geophys. Res. Atmos., 118, 8625-8639, 2013.

860 Li, J., Wang, G., Zhou, B., Cheng, C., Cao, J., Shen, Z., and An, Z.: Airborne particulate

861 organics at the summit (2060m, a.s.l.) of Mt. Hua in central China during winter: Implications for

862 biofuel and coal combustion, Atmos. Res., 106, 108-119,

863 https://doi.org/10.1016/j.atmosres.2011.11.012, 2012.

864 Li, Y. J., Lee, B., Yu, J., Ng, N., and Chan, C. K.: Evaluating the degree of oxygenation of

865 organic aerosol during foggy and hazy days in Hong Kong using high-resolution time-of-flight

866 aerosol mass spectrometry (HR-ToF-AMS), Atmos. Chem. Phys., 13, 8739-8753, 2013.

867 Liu, J., Zhang, F., Xu, W., Sun, Y., Chen, L., Li, S., Ren, J., Hu, B., Wu, H., and Zhang, R.:

868 Hygroscopicity of Organic Aerosols Linked to Formation Mechanisms, Geophys. Res. Lett., 48,

869   e2020GL091683, https://doi.org/10.1029/2020GL091683, 2021.

870   Liu, P., Song, M., Zhao, T., Gunthe, S. S., Ham, S., He, Y., Qin, Y. M., Gong, Z., Amorim, J.

871   C., Bertram, A. K., and Martin, S. T.: Resolving the mechanisms of hygroscopic growth and cloud

872   condensation nuclei activity for organic particulate matter, Nat. Commun., 9, 4076,

873   10.1038/s41467-018-06622-2, 2018.

874   Liu, P. F., Zhao, C. S., Göbel, T., Hallbauer, E., Nowak, A., Ran, L., Xu, W. Y., Deng, Z. Z.,

875   Ma, N., Mildenberger, K., Henning, S., Stratmann, F., and Wiedensohler, A.: Hygroscopic properties

876   of aerosol particles at high relative humidity and their diurnal variations in the North China Plain,

877   Atmos. Chem. Phys., 11, 3479-3494, 10.5194/acp-11-3479-2011, 2011.

878   Liu, X., and Wang, J.: How important is organic aerosol hygroscopicity to aerosol indirect

879   forcing?, Environ. Res. Lett., 5, 044010, 10.1088/1748-9326/5/4/044010, 2010.

880   Louvaris, E. E., Florou, K., Karnezi, E., Papanastasiou, D. K., Gkatzelis, G. I., and Pandis, S.

881   N.: Volatility of source apportioned wintertime organic aerosol in the city of Athens, Atmos.

882   Environ., 158, 138-147, https://doi.org/10.1016/j.atmosenv.2017.03.042, 2017.

883   Noziere, B.: Don't forget the surface, Science, 351, 1396-1397, 10.1126/science.aaf3253, 2016.

884   Ma, N., Zhao, C., Tao, J., Wu, Z., Kecorius, S., Wang, Z., Größ, J., Liu, H., Bian, Y., and Kuang,

885   Y.: Variation of CCN activity during new particle formation events in the North China Plain, Atmos.

886   Chem. Phys., 16, 8593-8607, 2016.

887   Massling, A., Stock, M., and Wiedensohler, A.: Diurnal, weekly, and seasonal variation of

888   hygroscopic properties of submicrometer urban aerosol particles, Atmos. Environ., 39, 3911-3922,

889   10.1016/j.atmosenv.2005.03.020, 2005.

890   Massoli, P., Lambe, A., Ahern, A., Williams, L., Ehn, M., Mikkilä, J., Canagaratna, M., Brune,

891   W., Onasch, T., and Jayne, J.: Relationship between aerosol oxidation level and hygroscopic

892   properties of laboratory generated secondary organic aerosol (SOA) particles, Geophys. Res. Lett.,

893   37, 2010.

894   May, A. A., Levin, E. J. T., Hennigan, C. J., Riipinen, I., Lee, T., Collett Jr., J. L., Jimenez, J.

895   L., Kreidenweis, S. M., and Robinson, A. L.: Gas-particle partitioning of primary organic aerosol

896   emissions: 3. Biomass burning, J. Geophys. Res. Atmos., 118, 11,327-311,338,

897   https://doi.org/10.1002/jgrd.50828, 2013.

898   Mei, F., Setyan, A., Zhang, Q., and Wang, J.: CCN activity of organic aerosols observed

899   downwind of urban emissions during CARES, Atmos. Chem. Phys., 13, 12155-12169, 2013.

900   Meng, J. W., Yeung, M. C., Li, Y. J., Lee, B. Y. L., and Chan, C. K.: Size-resolved cloud

901   condensation nuclei (CCN) activity and closure analysis at the HKUST Supersite in Hong Kong,

902   Atmos. Chem. Phys., 14, 10267-10282, 10.5194/acp-14-10267-2014, 2014.

903   Mochida, M., Kuwata, M., Miyakawa, T., Takegawa, N., Kawamura, K., and Kondo, Y.:

904   Relationship between hygroscopicity and cloud condensation nuclei activity for urban aerosols in

905   Tokyo, J. Geophys. Res., 111, D23204, 10.1029/2005jd006980, 2006.

906   Onasch, T. B., Trimborn, A., Fortner, E. C., Jayne, J. T., Kok, G. L., Williams, L. R., Davidovits,

907   P., and Worsnop, D. R.: Soot Particle Aerosol Mass Spectrometer: Development, Validation, and

908   Initial Application, Aerosol Sci. Tech., 46, 804-817, 10.1080/02786826.2012.663948, 2012.

909   Ovadnevaite, J., Zuend, A., Laaksonen, A., Sanchez, K. J., Roberts, G., Ceburnis, D., Decesari,

910   S., Rinaldi, M., Hodas, N., Facchini, M. C., Seinfeld, J. H., and O' Dowd, C.: Surface tension

911   prevails over solute effect in organic-influenced cloud droplet activation, Nature, 546, 637-641,

912   10.1038/nature22806, 2017.

913   Paatero, P., and Tapper, U.: Positive matrix factorization: A non-negative factor model with

914   optimal utilization of error estimates of data values, Environmetrics, 5, 111-126,

915   10.1002/env.3170050203, 1994.

916   Paatero, P.: Least squares formulation of robust non-negative factor analysis, Chemometr Intell

917   Lab, 37, 23-35, 10.1016/S0169-7439(96)00044-5, 1997.

918   Pajunoja, A., Lambe, A. T., Hakala, J., Rastak, N., Cummings, M. J., Brogan, J. F., Hao, L.,

919   Paramonov, M., Hong, J., and Prisle, N. L.: Adsorptive uptake of water by semisolid secondary

920   organic aerosols, Geophys. Res. Lett., 42, 3063-3068, 2015.

921   Park, S. H., Rogak, S. N., and Grieshop, A. P.: A Two-Dimensional Laminar Flow Model for

922   Thermodenuders Applied to Vapor Pressure Measurements, Aerosol Sci. Technol., 47, 283-293,

923   10.1080/02786826.2012.750711, 2013.

924   Petters, M., and Kreidenweis, S.: A single parameter representation of hygroscopic growth and

925   cloud condensation nucleus activity, Atmos. Chem. Phys., 7, 1961-1971, 2007.

926   Petters, M. D., Wex, H., Carrico, C. M., Hallbauer, E., Massling, A., McMeeking, G. R.,

927 Poulain, L., Wu, Z., Kreidenweis, S. M., and Stratmann, F.: Towards closing the gap between

928 hygroscopic growth and activation for secondary organic aerosol – Part 2: Theoretical approaches,

929 Atmos. Chem. Phys., 9, 3999-4009, 10.5194/acp-9-3999-2009, 2009.

930 Petters, M., and Kreidenweis, S.: A single parameter representation of hygroscopic growth and

931 cloud condensation nucleus activity–Part 3: Including surfactant partitioning, Atmos. Chem. Phys.,

932 13, 1081-1091, 2013.

933 Philippin, S., Wiedensohler, A., and Stratmann, F.: Measurements of non-volatile fractions of

934 pollution aerosols with an eight-tube volatility tandem differential mobility analyzer (VTDMA-8),

935 J. Aerosol Sci., 35, 185-203, http://dx.doi.org/10.1016/j.jaerosci.2003.07.004, 2004.

936 Qin, Y. M., Tan, H. B., Li, Y. J., Schurman, M. I., Li, F., Canonaco, F., Prévôt, A. S. H., and

937 Chan, C. K.: The role of traffic emissions in particulate organics and nitrate at a downwind site in

938 the periphery of Guangzhou, China, Atmos. Chem. Phys., 1-31, 2017.

939 Rastak, N., Pajunoja, A., Acosta Navarro, J. C., Ma, J., Song, M., Partridge, D. G., Kirkevåg,

940 A., Leong, Y., Hu, W. W., Taylor, N. F., Lambe, A., Cerully, K., Bougiatioti, A., Liu, P., Krejci, R.,

941 Petäjä, T., Percival, C., Davidovits, P., Worsnop, D. R., Ekman, A. M. L., Nenes, A., Martin, S.,

942 Jimenez, J. L., Collins, D. R., Topping, D. O., Bertram, A. K., Zuend, A., Virtanen, A., and Riipinen,

943 I.: Microphysical explanation of the RH-dependent water affinity of biogenic organic aerosol and

944 its importance for climate, Geophys. Res. Lett., 44, 5167-5177, 10.1002/2017GL073056, 2017.

945 Renbaum-Wolff, L., Song, M., Marcolli, C., Zhang, Y., Liu, P. F., Grayson, J. W., Geiger, F. M.,

946 Martin, S. T., and Bertram, A. K.: Observations and implications of liquid–liquid phase separation at high

947 relative humidities in secondary organic material produced by α-pinene ozonolysis without inorganic

948 salts, Atmos. Chem. Phys., 16, 7969-7979, 10.5194/acp-16-7969-2016, 2016.

949 Riipinen, I., Pierce, J. R., Donahue, N. M., and Pandis, S. N.: Equilibration time scales of

950 organic aerosol inside thermodenuders: Evaporation kinetics versus thermodynamics, Atmos.

951 Environ., 44, 597-607, https://doi.org/10.1016/j.atmosenv.2009.11.022, 2010.

952 Rose, D., Gunthe, S., Mikhailov, E., Frank, G., Dusek, U., Andreae, M. O., and Pöschl, U.:

953 Calibration and measurement uncertainties of a continuous-flow cloud condensation nuclei counter

954 (DMT-CCNC): CCN activation of ammonium sulfate and sodium chloride aerosol particles in theory

955 and experiment, Atmospheric Chemistry and Physics, 8, 1153-1179, 2008.

956   Rose, D., Nowak, A., Achtert, P., Wiedensohler, A., Hu, M., Shao, M., Zhang, Y., Andreae, M.

957   O., and Pöschl, U.: Cloud condensation nuclei in polluted air and biomass burning smoke near the

958   mega-city Guangzhou, China – Part 1: Size-resolved measurements and implications for the

959   modeling of aerosol particle hygroscopicity and CCN activity, Atmos. Chem. Phys., 10, 3365-3383,

960   10.5194/acp-10-3365-2010, 2010.

961   Ruehl, C. R. and Wilson, K. R.: Surface organic monolayers control the hygroscopic growth of

962   submicrometer particles at high relative humidity, The Journal of Physical Chemistry A, 118, 3952-3966,

963   2014.

964   Saha, P. K., Khlystov, A., Grieshop, A. P.: Determining aerosol volatility parameters using a

965   "Dual Thermodenuder" system: application to laboratory-generated organic aerosols, Aerosol Sci.

966   Tech., 49, 620-632, 2015.

967   Saha, P. K., Khlystov, A., Yahya, K., Zhang, Y., Xu, L., Ng, N. L., Grieshop, A. P.: Quantifying

968   the volatility of organic aerosol in the southeastern US, Atmos. Chem. Phys., 17, 501-520, 2017.

969   Saleh, R., Walker, J., and Khlystov, A.: Determination of saturation pressure and enthalpy of

970   vaporization of semi-volatile aerosols: The integrated volume method, J. Aerosol Sci.e, 39, 876-887,

971   https://doi.org/10.1016/j.jaerosci.2008.06.004, 2008.

972   Schill, G. P. and Tolbert, M. A.: Heterogeneous ice nucleation on phase-separated organic-sulfate

973   particles: effect of liquid vs. glassy coatings, Atmos. Chem. Phys., 13, 4681-4695, 10.5194/acp-13-4681-

974   2013, 2013.

975   Schill, G. P. and Tolbert, M. A.: Heterogeneous ice nucleation on phase-separated organic-sulfate

976   particles: effect of liquid vs. glassy coatings, Atmos. Chem. Phys., 13, 4681-4695, 10.5194/acp-13-4681-

977   2013, 2013.

978   Seinfeld, J. H., and Pandis, S. N.: Atmospheric chemistry and physics: from air pollution to

979   climate change, John Wiley & Sons, 2016.

980   Shrivastava, M., Cappa, C. D., Fan, J., Goldstein, A. H., Guenther, A. B., Jimenez, J. L., Kuang,

981   C., Laskin, A., Martin, S. T., Ng, N. L., Petaja, T., Pierce, J. R., Rasch, P. J., Roldin, P., Seinfeld, J.

982   H., Shilling, J., Smith, J. N., Thornton, J. A., Volkamer, R., Wang, J., Worsnop, D. R., Zaveri, R. A.,

983   Zelenyuk, A., and Zhang, Q.: Recent advances in understanding secondary organic aerosol:

984   Implications   for   global   climate   forcing,   Rev.   Geophys.,   55,   509-559,

985   https://doi.org/10.1002/2016RG000540, 2017.

986   Song, M., Marcolli, C., Krieger, U. K., Zuend, A., and Peter, T.: Liquid-liquid phase separation and

987   morphology of internally mixed dicarboxylic acids/ammonium sulfate/water particles, Atmos. Chem.

988   Phys., 12, 2691-2712, 10.5194/acp-12-2691-2012, 2012a.

989   Song, M., Marcolli, C., Krieger, U. K., Zuend, A., and Peter, T.: Liquid-liquid phase separation in

990   aerosol particles: Dependence on O:C, organic functionalities, and compositional complexity, Geophys.

991   Res. Lett., 39, https://doi.org/10.1029/2012GL052807, 2012b.

992   Stokes, R., and Robinson, R.: Interactions in aqueous nonelectrolyte solutions. I. Solute-

993   solvent equilibria, J. Phys. Chem., 70, 2126-2131, 1966.

994   Stolzenburg, M. R., and McMurry, P. H.: Equations Governing Single and Tandem DMA

995   Configurations and a New Lognormal Approximation to the Transfer Function, Aerosol Sci. Tech.,

996   42, 421-432, 10.1080/02786820802157823, 2008.

997   Sun, Y. L., Zhang, Q., Schwab, J. J., Yang, T., Ng, N. L., and Demerjian, K. L.: Factor analysis

998   of combined organic and inorganic aerosol mass spectra from high resolution aerosol mass

999   spectrometer measurements, Atmos. Chem. Phys., 12, 8537-8551, 10.5194/acp-12-8537-2012,

1000   2012.

1001   Tan, H., Xu, H., Wan, Q., Li, F., Deng, X., Chan, P. W., Xia, D., and Yin, Y.: Design and

1002   Application of an Unattended Multifunctional H-TDMA System, J. Atmos. Oceanic Tech., 30, 1136-

1003   1148, 10.1175/JTECH-D-12-00129.1, 2013a.

1004   Tan, H., Yin, Y., Gu, X., Li, F., Chan, P. W., Xu, H., Deng, X., and Wan, Q.: An observational

1005   study of the hygroscopic properties of aerosols over the Pearl River Delta region, Atmos. Environ.,

1006   77, 817-826, http://dx.doi.org/10.1016/j.atmosenv.2013.05.049, 2013b.

1007   Thalman, R., Sá, S. S. d., Palm, B. B., Barbosa, H. M., Pöhlker, M. L., Alexander, M. L., Brito,

1008   J., Carbone, S., Castillo, P., Day, D. A.: CCN activity and organic hygroscopicity of aerosols

1009   downwind of an urban region in central Amazonia: seasonal and diel variations and impact of

1010   anthropogenic emissions, Atmos. Chem. Phys., 17, 11779-11801, 2017.

1011   Ulbrich, I. M., Canagaratna, M. R., Zhang, Q., Worsnop, D. R., and Jimenez, J. L.:

1012   Interpretation of organic components from Positive Matrix Factorization of aerosol mass

1013   spectrometric data, Atmos. Chem. Phys., 9, 2891-2918, 10.5194/acp-9-2891-2009, 2009.

1014   Volkamer, R., Jimenez, J. L., Martini, F. S., Dzepina, K., Qi, Z., Salcedo, D., Molina, L. T.,

1015   Worsnop, D. R., and Molina, M. J.: Secondary organic aerosol formation from anthropogenic air

1016   pollution: Rapid and higher than expected, Geophys. Res. Lett., 33, 254-269, 2006.

1017   Wang, D. S., and Hildebrandt Ruiz, L.: Chlorine-initiated oxidation of n-alkanes under high-

1018   NOx conditions: insights into secondary organic aerosol composition and volatility using a

1019   FIGAERO–CIMS, Atmos. Chem. Phys., 18, 15535-15553, 10.5194/acp-18-15535-2018, 2018.

1020   Wang, J., Lee, Y. N., Daum, P. H., Jayne, J., and Alexander, M. L.: Effects of aerosol organics

1021   on cloud condensation nucleus (CCN) concentration and first indirect aerosol effect, Atmos. Chem.

1022   Phys., 8, 6325-6339, 10.5194/acp-8-6325-2008, 2008.

1023   Wang, J., Cubison, M., Aiken, A., Jimenez, J., and Collins, D.: The importance of aerosol

1024   mixing state and size-resolved composition on CCN concentration and the variation of the

1025   importance with atmospheric aging of aerosols, Atmos. Chem. Phys., 10, 7267-7283, 2010.

1026   Wex, H., Petters, M. D., Carrico, C. M., Hallbauer, E., Massling, A., McMeeking, G. R., Poulain,

1027   L., Wu, Z., Kreidenweis, S. M., and Stratmann, F.: Towards closing the gap between hygroscopic growth

1028   and activation for secondary organic aerosol: Part 1 – Evidence from measurements, Atmos. Chem. Phys.,

1029   9, 3987-3997, 10.5194/acp-9-3987-2009, 2009.

1030   Wu, Z. J., Poulain, L., Henning, S., Dieckmann, K., Birmili, W., Merkel, M., van Pinxteren,

1031   D., Spindler, G., Müller, K., Stratmann, F., Herrmann, H., and Wiedensohler, A.: Relating particle

1032   hygroscopicity and CCN activity to chemical composition during the HCCT-2010 field campaign,

1033   Atmos. Chem. Phys., 13, 7983-7996, 10.5194/acp-13-7983-2013, 2013.

1034   Xu, W., Chen, C., Qiu, Y., Xie, C., Chen, Y., Ma, N., Xu, W., Fu, P., Wang, Z., Pan, X., Zhu, J.,

1035   Ng, N. L., and Sun, Y.: Size-resolved characterization of organic aerosol in the North China Plain:

1036   new insights from high resolution spectral analysis, Environ. Sci. Atmos., 1, 346-358,

1037   10.1039/D1EA00025J, 2021.

1038   Xu, W., Xie, C., Karnezi, E., Zhang, Q., Wang, J., Pandis, S. N., Ge, X., Zhang, J., An, J., Wang,

1039   Q., Zhao, J., Du, W., Qiu, Y., Zhou, W., He, Y., Li, Y., Li, J., Fu, P., Wang, Z., Worsnop, D. R., and

1040   Sun, Y.: Summertime aerosol volatility measurements in Beijing, China, Atmos. Chem. Phys., 19,

1041   10205-10216, 10.5194/acp-19-10205-2019, 2019.

1042   Yuan, L., Zhang, X., Feng, M., Liu, X., Che, Y., Xu, H., Schaefer, K., Wang, S., and Zhou, Y.:

1043 Size-resolved hygroscopic behaviour and mixing state of submicron aerosols in a megacity of the

1044 Sichuan Basin during pollution and fireworks episodes, Atmos. Environ., 226, 117393,

1045 https://doi.org/10.1016/j.atmosenv.2020.117393, 2020.

1046 Zdanovskii, A.: NOVYI METOD RASCHETA RASTVORIMOSTEI ELEKTROLITOV V

1047 MNOGOKOMPONENTNYKH SISTEMAKH. 1, Zhurnal Fizicheskoi Khimii, 22, 1478-1485,

1048 1948.

1049 Zhang, Q., Canagaratna, M. R., Jayne, J. T., Worsnop, D. R., and Jimenez, J. L.: Time-and size-

1050 resolved chemical composition of submicron particles in Pittsburgh: Implications for aerosol

1051 sources and processes, J. Geophys. Res. Atmos., 1984–2012, 110, 2005a.

1052 Zhang, Q., Worsnop, D. R., Canagaratna, M. R., and Jimenez, J. L.: Hydrocarbon-like and

1053 oxygenated organic aerosols in Pittsburgh: insights into sources and processes of organic aerosols,

1054 Atmos. Chem. Phys., 5, 3289-3311, 10.5194/acp-5-3289-2005, 2005b.

1055 Zhang, Y., Tao, J., Ma, N., Kuang, Y., Wang, Z., Cheng, P., Xu, W., Yang, W., Zhang, S., Xiong,

1056 C., Dong, W., Xie, L., Sun, Y., Fu, P., Zhou, G., Cheng, Y., and Su, H.: Predicting cloud condensation

1057 nuclei number concentration based on conventional measurements of aerosol properties in the North

1058 China Plain, Sci. Tot. Environ., 719, 137473, https://doi.org/10.1016/j.scitotenv.2020.137473, 2020.

1059 Zhao, D. F., Buchholz, A., Kortner, B., Schlag, P., Rubach, F., Kiendler-Scharr, A., Tillmann,

1060 R., Wahner, A., Flores, J. M., Rudich, Y., Watne, Å. K., Hallquist, M., Wildt, J., and Mentel, T. F.:

1061 Size-dependent hygroscopicity parameter (κ) and chemical composition of secondary organic cloud

1062 condensation nuclei, Geophys. Res. Lett., 42, 10,920-910,928,

1063 https://doi.org/10.1002/2015GL066497, 2015.

1064 Zhao, D. F., Buchholz, A., Kortner, B., Schlag, P., Rubach, F., Fuchs, H., Kiendler-Scharr, A.,

1065 Tillmann, R., Wahner, A., Watne, Å. K., Hallquist, M., Flores, J. M., Rudich, Y., Kristensen, K.,

1066 Hansen, A. M. K., Glasius, M., Kourtchev, I., Kalberer, M., and Mentel, T. F.: Cloud condensation

1067 nuclei activity, droplet growth kinetics, and hygroscopicity of biogenic and anthropogenic

1068 secondary organic aerosol (SOA), Atmos. Chem. Phys., 16, 1105-1121, 10.5194/acp-16-1105-2016,

1069 2016.

1070

1071 Table 1. The density and the κ value of the related species used in this study.

Species	Density (kg m^{-3})	κ
NH_4NO_3	1720[a]	0.58[b]
NH_4HSO_4	1780[a]	0.56[b]
H_2SO_4	1830[a]	0.90[b]
$(NH_4)_2SO_4$	1769[a]	0.48[b]
Organics	1400[a]	0.10[b]
BC	1770[c]	0[d]

1072 [a] From Gysel et al. (2007); [b] From (Cai et al., 2018); [c] From Deng et al. (2019); [d] Assumed to be 0.

1073

1074 Table 2. Thermophysical properties of each component used in the multi-component evaporation

1075 dynamics model.

Parameters	ELVOA	LVOA	SVOA	Ammonium Nitrate	Ammonium Sulfate	Black Carbon
$C_i^*(T_{ref})$ ($\mu g\ m^{-3}$) [a]	10^{-5}	10^{-2}	10	76	2×10^{-3}	10^{-30}
D_i ($m^2\ s^{-1}$) [b]	5×10^{-6}	5×10^{-6}	5×10^{-6}	5×10^{-6}	5×10^{-6}	5×10^{-6}
$\sigma_{s/a}$ ($N\ m^{-1}$) [c]	0.05	0.05	0.05	0.05	0.05	0.05
M_i ($kg\ mol^{-1}$)	0.2	0.2	0.2	0.08	0.132	0.28
ρ_i ($kg\ m^{-3}$)	1400	1400	1400	1720	1769	1770
$\Delta H_{vap,i}$ ($kJ\ mol^{-1}$) [d]	80	80	80	152	94	100
α [e]	0.09	0.09	0.09	0.09	0.09	0.09

1076 [a] From Hong et al. (2017); [b] From Riipinen et al. (2010); [c] From Riipinen et al. (2010); [d] The ΔH_{vap}

1077 values of organics are obtained from the sensitivity test shown in Fig. S4 and the values of inorganic

1078 species are from Hong et al. (2017); [e] Obtained from the sensitivity test shown in Fig. S4.

1079

1080   Table 3. The average and standard deviation values (mean±std) of N_{CCN}, AR, D_{50}, and κ_{CCN} at 0.1%,

1081   0.2%, 0.4%, 0.7%, 0.9% and 1.0% SS during the campaign.

SS	0.1%	0.2%	0.4%	0.7%	0.9%	1.0%
N_{CCN} (# cm^{-3})	2507±1187	4322±1981	5843±2461	6834±2921	7497±3210	7862±3352
AR	0.20±0.09	0.34±0.13	0.45±0.16	0.52±0.17	0.57±0.17	0.60±0.17
D_{50} (nm)	145.55±11.26	92.83±8.80	66.79±6.33	52.56±5.46	45.38±4.82	42.26±4.45
κ_{CCN}	0.48±0.13	0.47±0.15	0.31±0.10	0.22±0.09	0.20±0.08	0.20±0.08

1082

1083   FIGURE CAPTIONS

1084   Figure 1. The temporal profile of the measured variables during the campaign. (a) particle number

1085   size distribution; (b) PM_1 chemical composition measured by the SP-AMS along with mass

1086   concentration of $PM_{2.5}$; (c) mass fraction of each species; (d) wind speed and direction. The color

1087   code in (d) represents the wind direction.

1088   Figure 2. The temporal profile of GF-PDF at the measured diameters (30, 50, 80, 100, 150 and 200

1089   nm). The color code denotes the probability density and the red solid line represents the mean GF

1090   (GF_{mean}).

1091   Figure 3. The average mass fraction distribution of SVOA, LVOA and ELVOA at the measured

1092   diameters (30, 50, 80, 100, 150 and 200 nm), and average size-resolved hygroscopicity of organic

1093   aerosol (κ_{OA}) with the upper and lower error bars (in red).

1094   Figure 4. The campaign average diurnal variation of mass fraction of organics and f44 in bulk

1095 PM_1 (a), the κ values at 200 nm obtained by HTDMA (κ_{HTDMA}) and AMS (κ_{AMS}) measurements

1096   (b), the PNSD (c) and mass distribution of organics (d). The shaded area represents standard

1097   deviation.

1098   Figure 5. The diurnal variation (displayed in boxplot) mass concentration of the deconvolved OA

1099   factors from PMF analysis of AMS data, including more oxygenated OA (MOOA), less

1100   oxygenated OA (LOOA), aged biomass burning OA (aBBOA), hydrocarbon-like OA (HOA),

1101   biomass burning OA (BBOA), and nighttime OA (night-OA).

1102   Figure 6. The average (solid line) and standard deviation (shaded area) diurnal variation of κ_{OA} at

1103   different particle diameters.

1104   Figure 7. The size-resolved volatility distribution during daytime (8:00-16:00 LT) and nighttime

1105   (20:00 to 4:00 LT) based on the median time of each cycle owing to the limited time resolution.

1106   Figure 8. The average diurnal variation of $\delta_{N_{CCN}}$ at 0.1%, 0.2%, 0.4% and 0.7% SS based on fixed

1107 κ_{OA} (a), SR κ_{OA} (b) and SR diurnal κ_{OA} (c).

1108
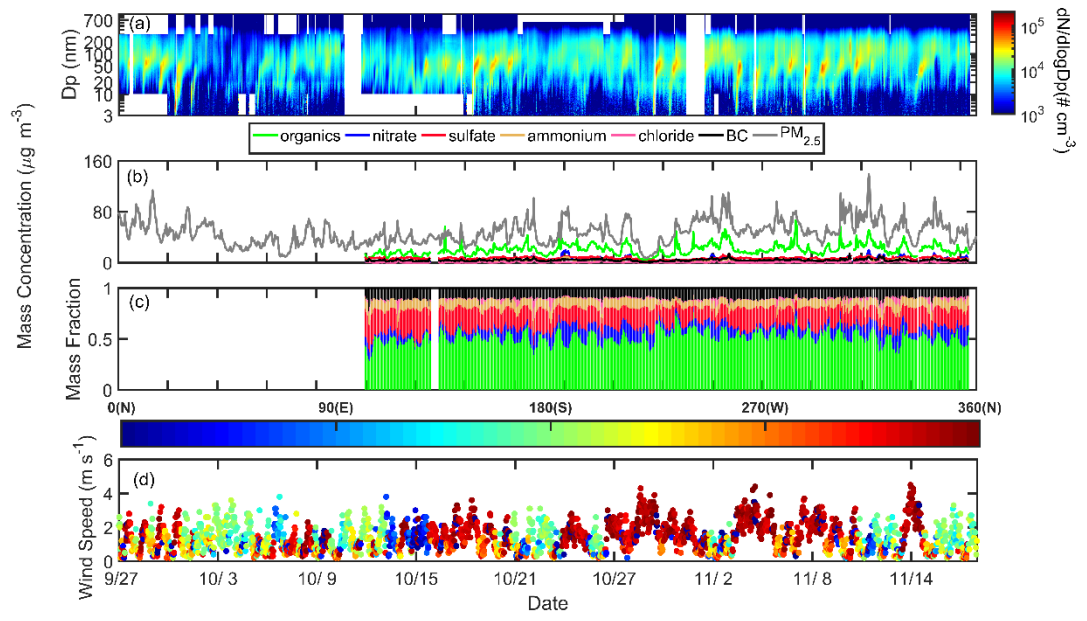
1109

1110

1111

1112   Fig. 1.

1113
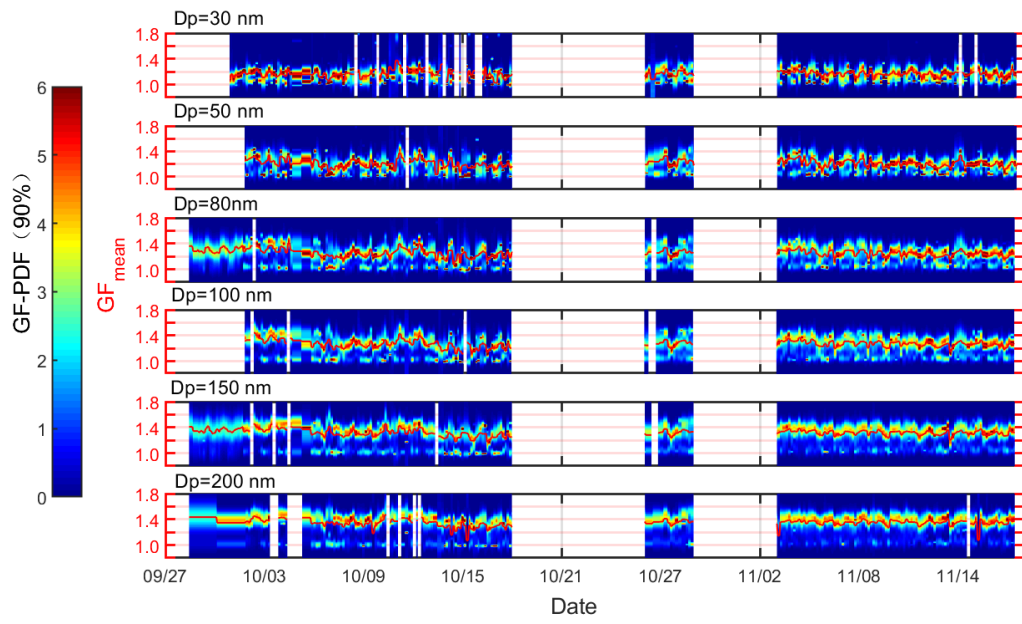
1114

1115   Fig. 2.

1116
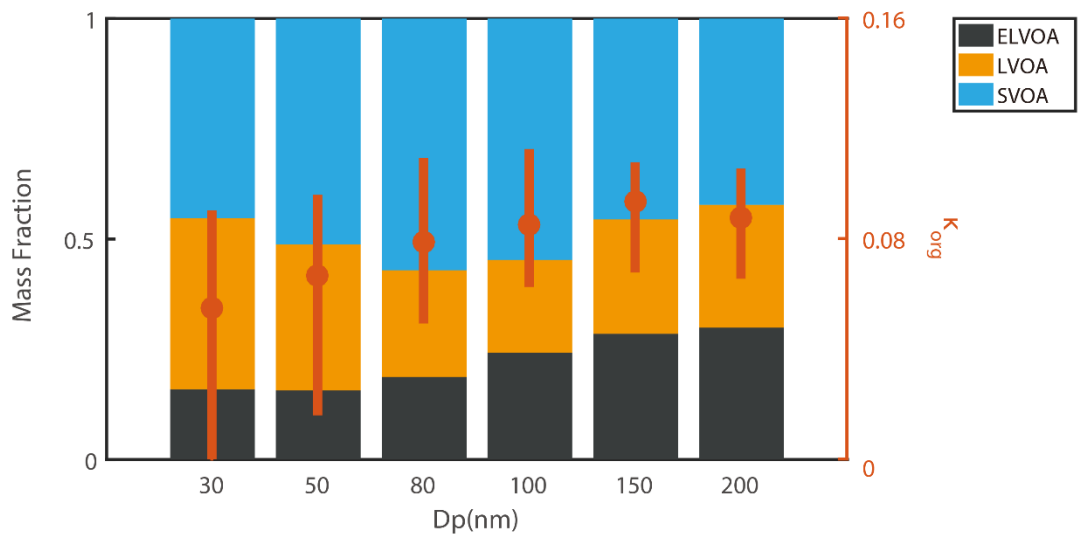
1117

1118

1119   Fig. 3.

1120
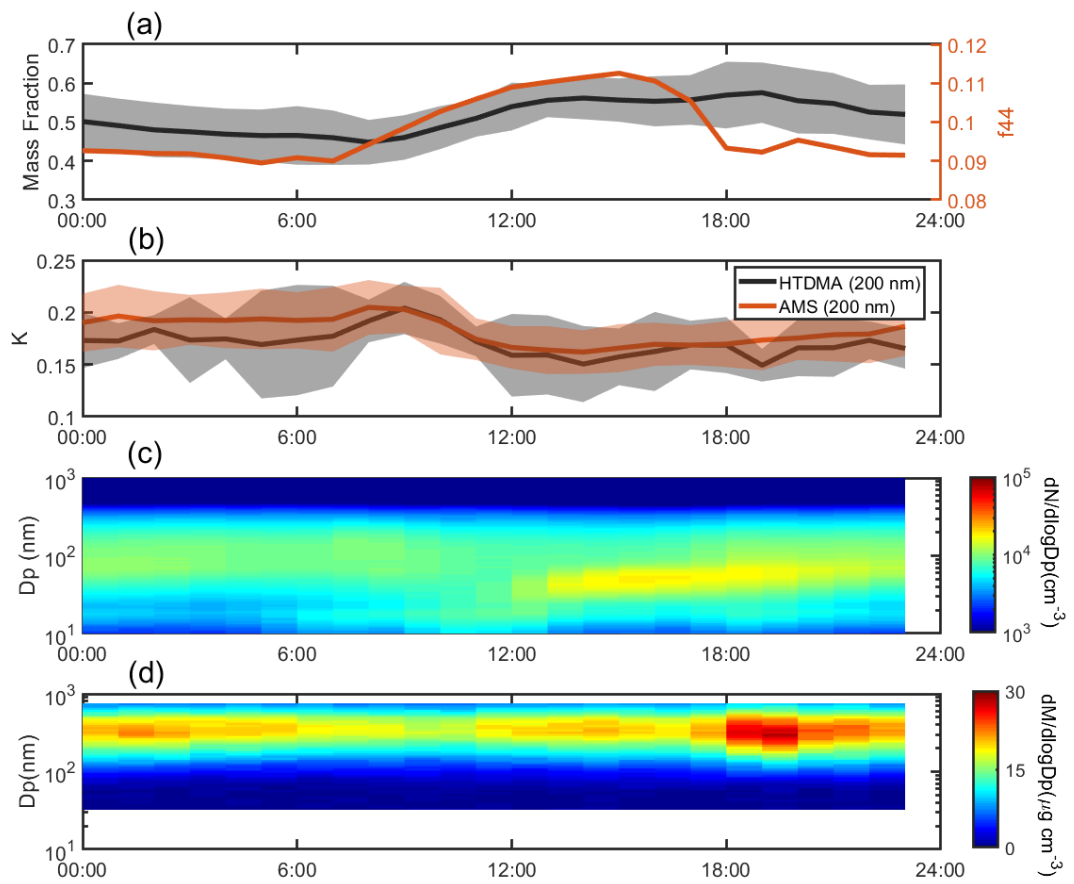
1121

1122

1123   Fig. 4.

1124
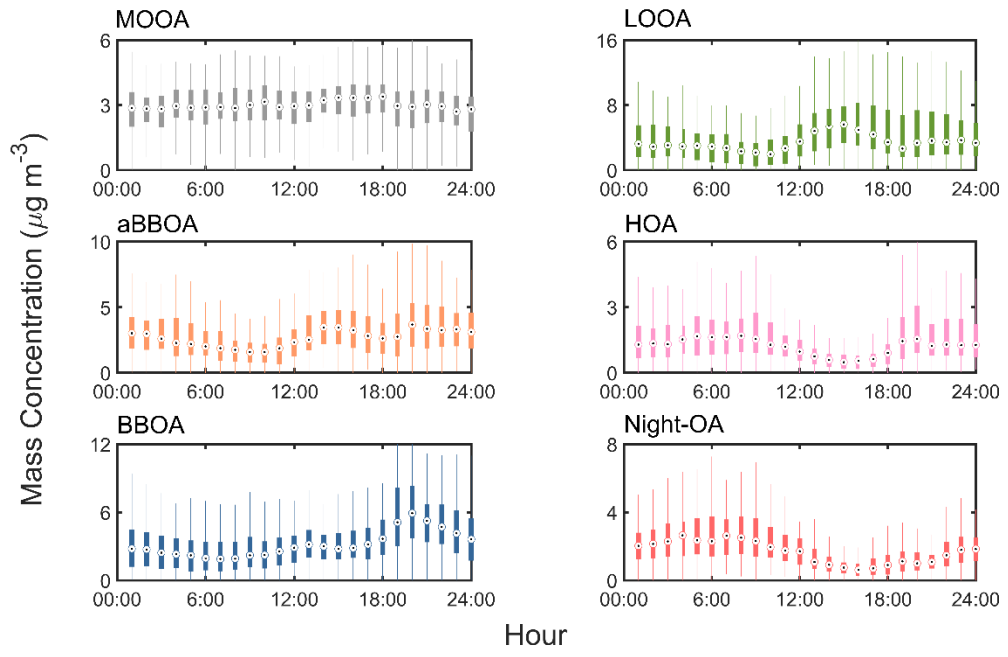
1125

1126

1127   Fig. 5.
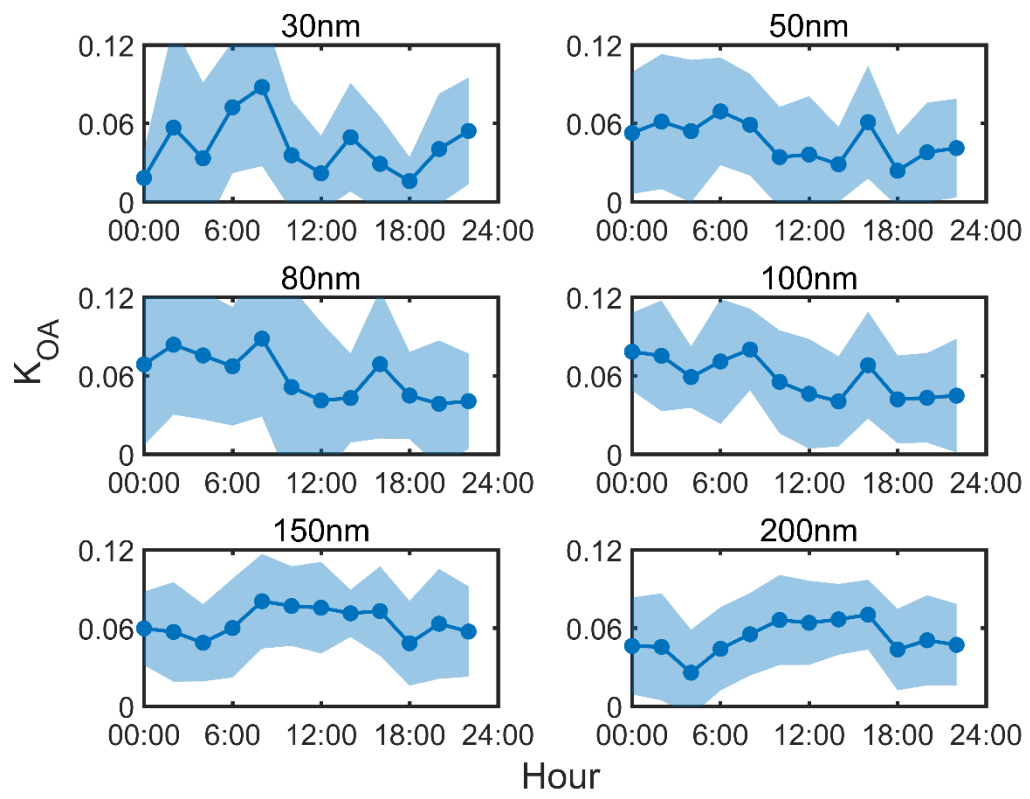
1128

1129

1130   Fig. 6.
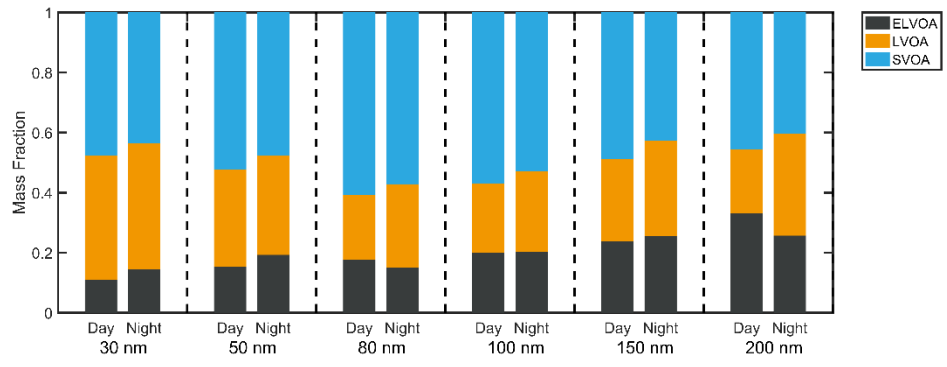
1131

1132

1133  Fig. 7.

1134

1135

1136

1137

1138   Fig. 8.